

REPORT DOCUMENTATION PAGE			<i>Form Approved</i> <i>OMB No. 0704-0188</i>	
Public reporting burden for this collection of information is estimated to average 1 hour per response, including the time for reviewing instructions, searching existing data sources, gathering and maintaining the data needed, and completing and reviewing this collection of information. Send comments regarding this burden estimate or any other aspect of this collection of information, including suggestions for reducing this burden to Department of Defense, Washington Headquarters Services, Directorate for Information Operations and Reports (0704-0188), 1215 Jefferson Davis Highway, Suite 1204, Arlington, VA 22202-4302. Respondents should be aware that notwithstanding any other provision of law, no person shall be subject to any penalty for failing to comply with a collection of information if it does not display a currently valid OMB control number. PLEASE DO NOT RETURN YOUR FORM TO THE ABOVE ADDRESS.				
1. REPORT DATE (DD-MM-YYYY) 02-07-2012		2. REPORT TYPE Final		3. DATES COVERED (From - To) April 2009-November 2011
4. TITLE AND SUBTITLE MULTI-SCALE MICROSTRUCTURE AND MECHANICAL PROPERTIES OF HIGH CARBON EUTECTIC TANTALUM CARBIDE REINFORCED WITH CARBON NANOTUBES			5a. CONTRACT NUMBER	
			5b. GRANT NUMBER FA9550-09-1-0297	
			5c. PROGRAM ELEMENT NUMBER	
6. AUTHOR(S) Arvind Agarwal			5d. PROJECT NUMBER	
			5e. TASK NUMBER	
			5f. WORK UNIT NUMBER	
7. PERFORMING ORGANIZATION NAME(S) AND ADDRESS(ES) Florida International University College of Engineering and Computing 10555 West Flagler Street, Miami, FL 33174			8. PERFORMING ORGANIZATION REPORT NUMBER	
9. SPONSORING / MONITORING AGENCY NAME(S) AND ADDRESS(ES) Dr. Ali Sayir Air Force Office of Scientific Research 875 North Randolph Street Arlington, VA 22203 ali.sayir@afosr.af.mil			10. SPONSOR/MONITOR'S ACRONYM(S)	
			11. SPONSOR/MONITOR'S REPORT NUMBER(S) AFRL-OSR-VA-TR-2012-0531	
12. DISTRIBUTION / AVAILABILITY STATEMENT Available to public-A				
13. SUPPLEMENTARY NOTES				
14. ABSTRACT The overall objective was to develop multiwall carbon nanotube (CNT) reinforced TaC composite with an understanding of mechanical properties at multiple length scales. Spark plasma sintering technique was employed to consolidate fully dense TaC reinforced with nano B4C and carbon nanotubes with varying lengths. Oxidation behavior of TaC, TaC-B4C and TaC-CNT composites was evaluated by exposing them to high temperature DC plasma plume at temperatures close to 2000 C. TaC and TaC-CNT composites displayed comparable oxidation resistance which was 15 times better than TaC-B4C composites. CNT addition restricted grain growth by pinning. Transverse Rupture Strength of TaC reinforced with shorter CNTs (1-2 um long) displayed highest strength/density ratio with an improvement of 65% as compared to pure TaC. This was attributed to strengthening caused by CNTs and transformation of shorter CNTs into graphene nano platelets.				
15. SUBJECT TERMS				
16. SECURITY CLASSIFICATION OF:			17. LIMITATION OF ABSTRACT	18. NUMBER OF PAGES 35
a. REPORT UU	b. ABSTRACT UU	c. THIS PAGE UU		
			19b. TELEPHONE NUMBER (include area code)	

Multi-Scale Microstructure and Mechanical Properties of High Carbon Eutectic Tantalum Carbide Reinforced with Carbon Nanotubes

Final Report

FA9550-09-1-0297

PI: Arvind Agarwal

Professor

Department of Mechanical and Materials Engineering

Florida International University

10555 West Flagler Street, EC 3464

Miami, FL 33174

Phone: 305-348-1701, Fax: 305-348-1932

<http://web.eng.fiu.edu/agarwala>

Email: agarwala@fiu.edu

Abstract

The overall objective was to develop multiwall carbon nanotube (CNT) reinforced TaC composite with an understanding of mechanical and oxidation properties. Spark plasma sintering was employed to consolidate TaC reinforced with nano B₄C and carbon nanotubes. TaC and TaC-1 wt.% B₄C powders were consolidated using spark plasma sintering (SPS) at 1850 °C and varying pressure of 100, 255 and 363 MPa. Addition of B₄C leads to an increase in the density of 100 MPa sample from 89% to 97%. B₄C nano-powder resists grain growth even at high pressure of 363 MPa. Relative fracture toughness increased by up to 93% on B₄C addition. TaC-4 wt.% CNT composites were synthesized using two kinds of CNTs, having long (10-20 μm) and short (1-3 μm) length. Addition of CNTs leads to an increase in the density of 100 MPa sample from 89% to 95%. Short CNTs are more effective in increasing the density of the composites whereas long CNTs are more effective grain growth inhibitors. Transverse Rupture Strength of TaC reinforced with shorter CNTs displayed highest strength/density ratio with an improvement of 65% as compared to pure TaC. This was attributed to strengthening caused by CNTs and transformation of shorter CNTs into graphene nano platelets. Oxidation behavior of TaC, TaC-B₄C and TaC-CNT composites was evaluated by exposing them to high temperature DC plasma plume at temperatures close to 2000⁰C. TaC and TaC-CNT composites displayed comparable oxidation resistance which was 15 times better than TaC-B₄C composites.

Major Findings:

We have demonstrated that multiwall carbon nanotube (CNT) reinforced Tantalum Carbide (TaC) can be successfully synthesized by spark plasma sintering. The following objectives were achieved:

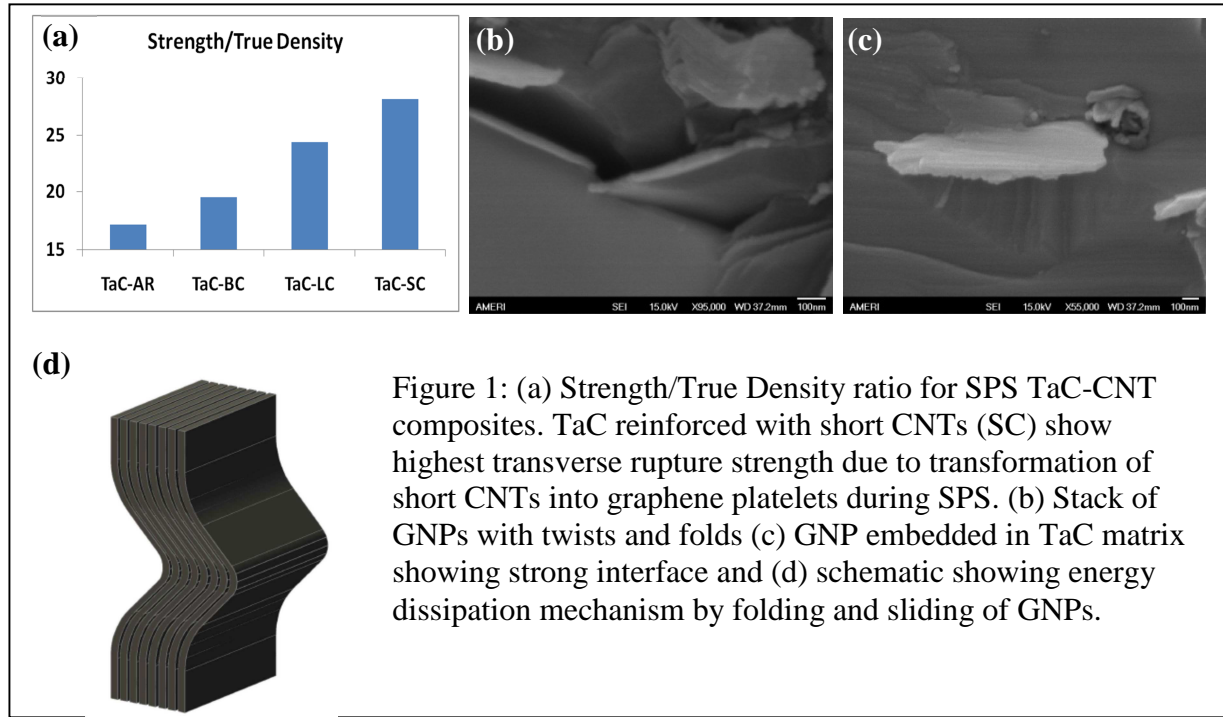
1. Successful *dispersion* of CNTs in the TaC matrix by three methods *viz.* wet chemistry, spray drying and chemical vapor growth.
2. Successful *consolidation* of TaC-CNT composites by spark plasma sintering. Addition of 4 wt.% CNT leads to an increase in the density of TaC from 89% to 95%.
3. CNTs *restricted grain growth* in TaC by grain boundary pinning. TaC *grain size reduced* from 5.6 μm to 1.2 μm with CNT addition for the same sintering conditions.
4. Fracture toughness *enhancement up to 60%* was observed on CNT addition.
5. Modeling of stress in TaC was investigated by object oriented finite element method and mesh free method as a function of microstructural features.
6. *Strength to density ratio* of CNT reinforced TaC increased from 17 to 28, which is an increase of $\sim 65\%$.
7. Oxidation behavior of TaC, TaC-B₄C and TaC-CNT composites was evaluated by exposing them to high temperature DC plasma plume at temperatures close to 2000^oC. TaC and TaC-CNT composites displayed comparable oxidation resistance which was 15 times better than TaC-B₄C composites.

The findings 1-5 listed above have been published in form of three (3) journal articles which are attached with this report. Findings 6 and 7 are being prepared as journal manuscripts at the time of submission of this report. The results of findings 6 and 7 are shown in detail below.

Finding 6: High Strength to Density ratio of CNT Reinforced TaC

We learnt some interesting lessons from research on spark plasma sintered TaC with CNT reinforcement. Two kinds of CNTs, having long (10-20 μm) and short (1-3 μm) length, were added to synthesize TaC-4 wt.% CNT composite. Based on the conventional understanding of the composite materials, it was expected that TaC with longer CNTs would evince higher fracture strength as longer fiber can carry larger load. On the contrary, higher rupture strength (330 MPa) was observed in short CNT reinforced TaC (TaC-SC) in comparison to long CNT reinforced (TaC-LC) as shown in the bar chart (Figure 1a) below. TaC-SC shows a 16% increase in the rupture strength over TaC-LC. This *intriguing* result followed by detailed SEM investigation lead to the conclusion that shorter CNTs were transformed into Graphene nanoplatelets (GNP) during SPS and demonstrated novel strengthening mechanisms, which has not been observed earlier in ceramic matrix composites. Figure 1b shows a stack of GNPs with twists and folds, trapped between TaC grains. Fig 1c shows a GNP pullout from TaC grains. Both microstructures are indicative of the higher energy dissipation mechanisms. Firstly, the bends, folds and interlayer sliding (Figure 1b) in GNP results in the absorption of the fracture energy. This is a very unique mechanism and is not commonly observed in ceramics. Secondly, the pull-out energy of a GNP sheet (Figure 1c) from the matrix is estimated to be higher than a nanotube/fiber due to “sheet wrapping” phenomenon. A similar result has been observed in recently published work on Si₃N₄-Graphene composites. Thus, graphene owing to its excellent elastic modulus (0.5-1 TPa) and tensile strength (130 GPa), has immense potential to increase the elastic modulus and strength, when used as reinforcement in a ceramic composite structure.

The strengthening caused by GNP was more effective than CNTs. Hence, the idea of reinforcing TaC with GNP was born. GNPs are very inexpensive than carbon nanotubes and readily available in the large amount. The toughening mechanism is elucidated schematically in Figure 1d.



Finding 7: Oxidation Resistance of Spark Plasma Sintered TaC

Experimental Procedure: Oxidation studies were carried out on the rectangular samples which were machined from the SPS pellets which were ~ 4-6 mm thick and 20 mm in diameter. Dimensions and nomenclature of the machined samples are shown in Table-1. The average grain size and density of three compositions of TaC are also included in Table-1.

Table 1: Dimensions of TaC based samples for oxidation studies

Sample Id	Sample Composition	Dimensions (mm)	Relative Density (%)	Grain Size (μm)
TaC	TaC	18.7×4.3×1.70	89	0.56 ± 0.12
TaC-BC	TaC-1 wt.% B ₄ C	16.4×4.1×1.10	97	1.18 ± 0.39
TaC-LC	TaC- 4 wt.% long CNT	16.1×5.7×1.21	95	0.61 ± 0.27

A fixture was designed and machined using pure tungsten (W) to withstand extremely high temperature from exposure to the plasma jet. Figure 2a shows the front and back (inset image) of the fixture. TaC based sample was firmly held in the tungsten fixture. A small hole ($\text{\O} = 1 \text{ mm}$) was drilled into the back face of the fixture below 1-2 mm below the fixture edge, as shown in inset of Figure 2a. A K-type thermocouple (KMQSS-020U, Omega Engineering Inc.) was inserted in this hole which touches the lower and rear end of the sample to continuously monitor the temperature during the oxidation test. The rear location was selected to insert thermocouple to prevent it from getting burnt during exposure to the plasma jet. SG 100 DC plasma spray gun (Praxair, Danbury, CT, USA) was used for carrying out the plasma oxidation studies. Figure 2b shows the plasma spray set-up for the oxidation study. Table 2 illustrates the process parameters at which plasma oxidation test were carried out. During the plasma oxidation studies, plasma gun was positioned in front of the sample at 50 mm stand-off distance. The temperature of the particles emitted from plasma at 50 mm stand-off location was measured using AccuraSpray™ in-flight diagnostic sensor (Tecnar Automation Ltée, QC, Canada). Temperature of the particle is measured by two color pyrometry. Accuraspray experiments were conducted without TaC sample in the fixture. The prime reason to conduct such experiment was to get an idea about the temperature range at the front face of TaC sample. As stated earlier, thermocouple could not be inserted near front surface as it will melt in high temperature plasma. Accuraspray recorded a temperature of 2800 K for the processing parameters listed in Table 2. Hence, it can be safely concluded that front face of the TaC samples experienced temperatures greater than 2000 °C, which is a critical requirement for ultrahigh temperature application. TaC samples were exposed to such extreme conditions of plasma jet for a period of 30 seconds.

Table 2: Process parameters for plasma oxidation studies

Plasma power (kW)	Stand-off distance (mm)	Primary gas (Argon) flow rate (psi)	Secondary gas (Helium) flow rate (psi)	Spray time (seconds)
32	50	40	80	30

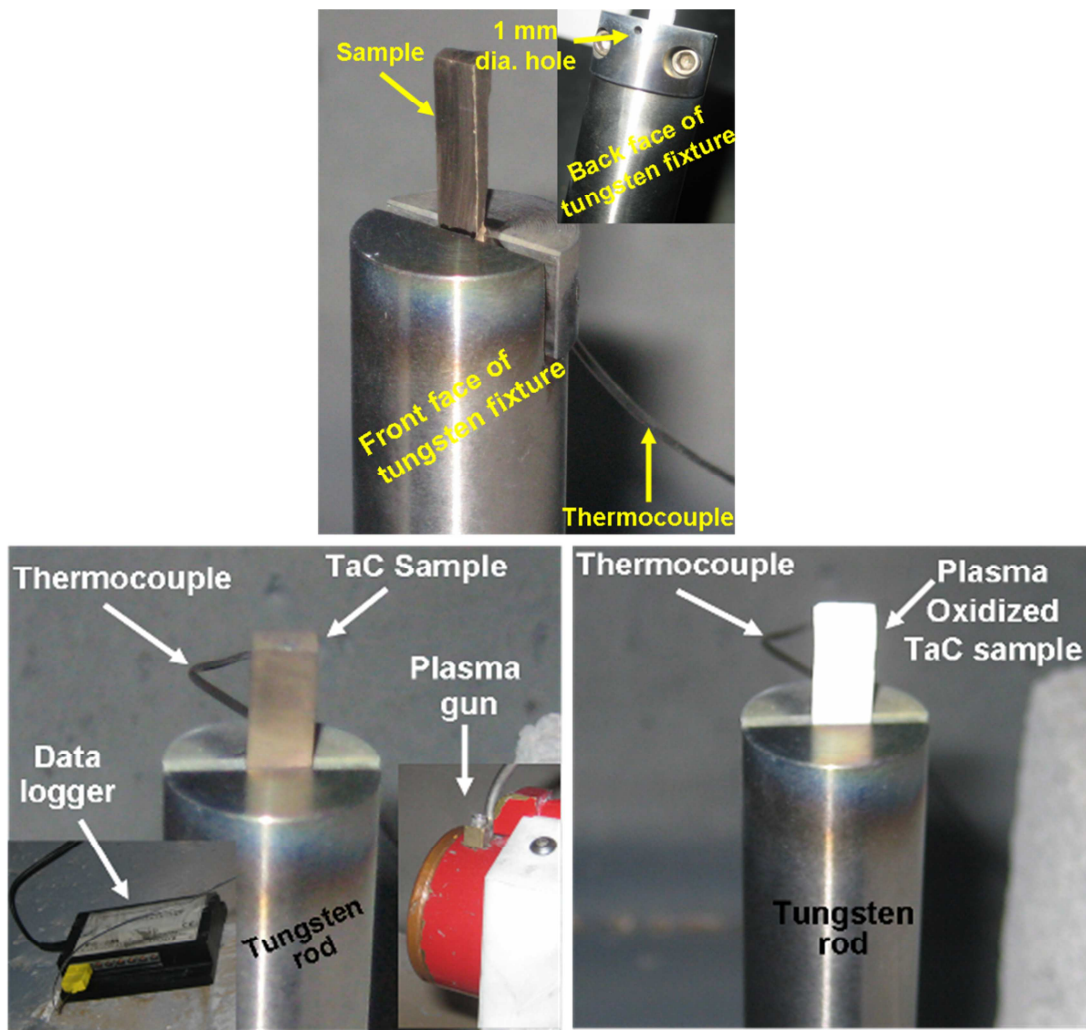


Figure 2: (a) Digital picture of tungsten fixture showing its front and back face (inset). (b) Plasma spray set-up before the plasma oxidation test (c) plasma oxidized TaC sample after the oxidation test.

Result and Discussion:

The average thickness of the oxide layer in each composition was measured from several such cross-sectional images and plotted in Fig 3. The oxide layer thickness of pure TaC and TaC-LC is thin and similar (25-28 μm) whereas TaC-BC shows a very thick oxide layer of 444 μm after plasma exposure. The top surface of the oxide layer was also examined to understand the oxide formation. Figure 4 shows the low and high magnification SEM images of the oxide morphologies of TaC, TaC-BC and TaC-LC samples. Oxidized surface of pure TaC sample (Fig 4(a) and Fig 4 (a-1)) shows porous and faceted microstructure which might be caused by ablation during high temperature plasma exposure. The surface morphology of TaC-BC sample showed a completely different topography which looks like “popcorn-like” indicating higher internal

pressure of the material. TaC-LC sample shows a finer grained oxide structure with uniform porosity in the inter-particle region. Oxide surfaces in TaC and TaC-BC samples also showed more severe crack formation as compared to TaC-LC. Addition of nano B₄C into TaC cause a significant change in the microstructure of oxide layer. A large number of pores were found in TaC-BC oxide layer. B₄C reacts with oxygen to produce B₂O₃ at the temperature over 1000°C. B₂O₃ easily evaporates to transform into gas phase leaving more pores for oxygen ingress and higher oxidation.

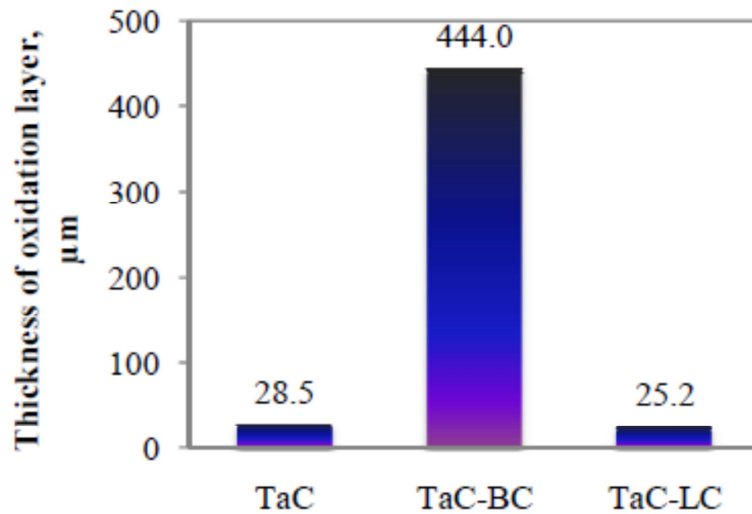


Figure 3. Thickness of oxidized layer section of different TaC samples

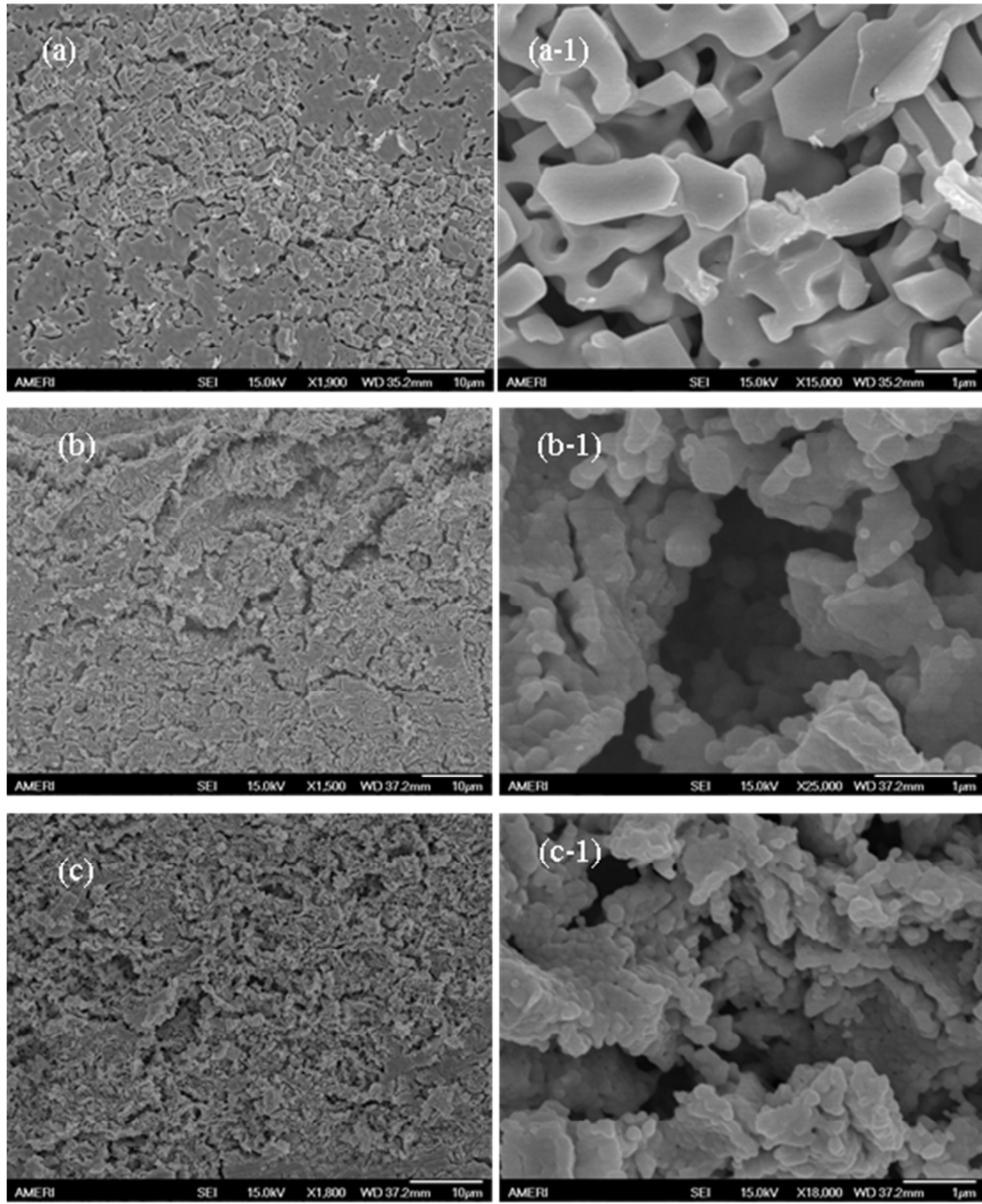


Figure 4. SEM observation of the oxide surface morphologies of various TaC samples after oxidation (a) (a-1) pure TaC; (b) (b-1) TaC-BC and ; (c) (c-1) TaC-LC samples

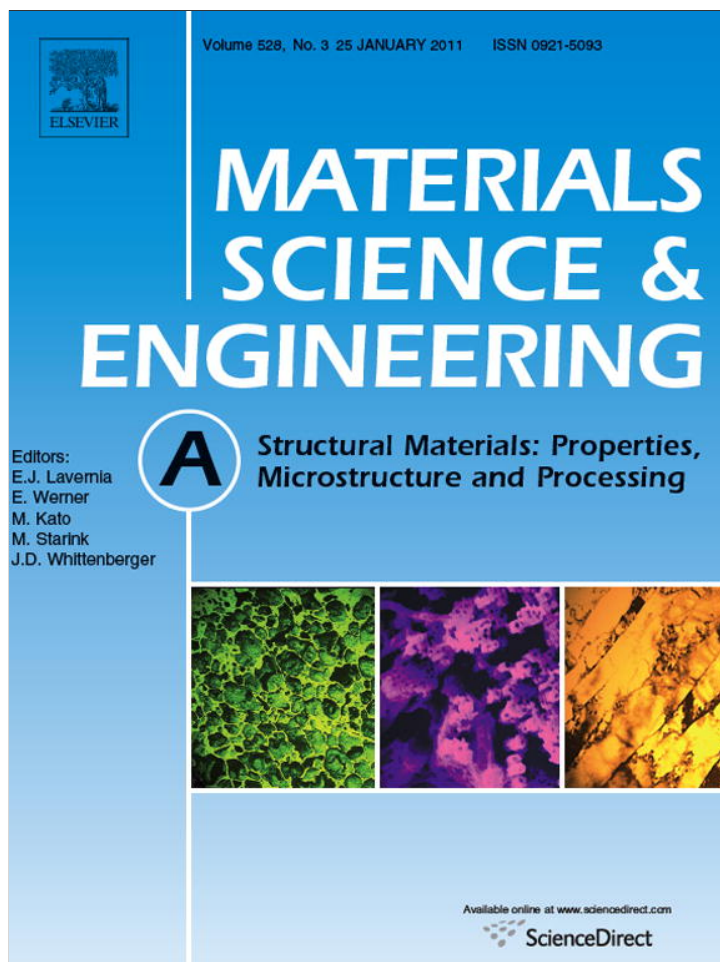
Published Journal Articles

1. S.R. Bakshi, V. Musaramthota, D. Lahiri, V. Singh, S. Seal and Arvind Agarwal, “Spark Plasma Sintered Tantalum Carbide: Effect of Pressure and Carbon Nanotube Addition on Microstructure and Mechanical Properties”, *Mater. Sci. Eng. A.*, Vol. 528, pp. 2538-2547, 2011.
2. S.R. Bakshi, V. Musaramthota, D. Lahiri, V. Singh, S. Seal and Arvind Agarwal, “Spark Plasma Sintered Tantalum Carbide: Effect of Pressure and nano Boron Carbide Addition on Microstructure and Mechanical Properties”, *Mater. Sci. Eng. A.*, vol. 528, Issue 3, pp.1287-1295, 2011.
3. S. R. Bakshi, A. Bhargava, S. Mohammadizadeh, I. Tsukanov and Arvind Agarwal, “Computational Estimation of Elastic Properties of Spark Plasma Sintered Tantalum Carbide by Meshfree and Finite Element Methods”, *Comp. Mater. Sci.*, Vol. 50, pp. 2615-2620, 2011.

Under Preparation:

1. D. Lahiri, E. Khaleghi, S. R. Bakshi, E. A. Olevsky, and Arvind Agarwal, “Strengthening Effect of Graphene Nanoplatelet Formation in Spark Plasma Sintered Tantalum Carbide-Nanotube Composite”, *to be submitted to Scripta Mater.*
2. M. Bao, D. Lahiri, A.K. Keshri, C. Zhang, S. R. Bakshi and Arvind Agarwal, “Oxidation Behavior of TaC based Composites in High Temperature Plasma”, *to be submitted to J. Amer Ceram. Soc.*

Provided for non-commercial research and education use.
Not for reproduction, distribution or commercial use.



This article appeared in a journal published by Elsevier. The attached copy is furnished to the author for internal non-commercial research and education use, including for instruction at the authors institution and sharing with colleagues.

Other uses, including reproduction and distribution, or selling or licensing copies, or posting to personal, institutional or third party websites are prohibited.

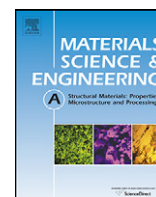
In most cases authors are permitted to post their version of the article (e.g. in Word or Tex form) to their personal website or institutional repository. Authors requiring further information regarding Elsevier's archiving and manuscript policies are encouraged to visit:

<http://www.elsevier.com/copyright>



Contents lists available at ScienceDirect

Materials Science and Engineering A

journal homepage: www.elsevier.com/locate/msea

Spark plasma sintered tantalum carbide: Effect of pressure and nano-boron carbide addition on microstructure and mechanical properties

Srinivasa R. Bakshi^a, Vishal Musaramthota^a, Debrupa Lahiri^a, Virendra Singh^b, Sudipta Seal^b, Arvind Agarwal^{a,*}

^a Plasma Forming Laboratory, Nanomechanics and Nanotribology Laboratory, Department of Mechanical and Materials Engineering, Florida International University, Miami, FL 33174, USA

^b AMPAC and Nanoscience Technology Center, University of Central Florida, Orlando, FL 32816, USA

ARTICLE INFO

Article history:

Received 18 July 2010

Received in revised form 6 October 2010

Accepted 6 October 2010

Keywords:

Tantalum carbide

Boron carbide

Spark plasma sintering

Grain growth

Densification

ABSTRACT

TaC and TaC–1 wt.% B₄C powders were consolidated using spark plasma sintering (SPS) at 1850 °C and varying pressure of 100, 255 and 363 MPa. The effect of pressure on the densification and grain size is evaluated. The role of nano-sized B₄C as sintering aid and grain growth inhibitor is studied by means of XRD, SEM and high resolution TEM. Fully dense TaC samples were produced at a pressure of 255 MPa and higher at 1850 °C. The increasing pressure also resulted in an increase in TaC grain size. Addition of B₄C leads to an increase in the density of 100 MPa sample from 89% to 97%. B₄C nano-powder resists grain growth even at high pressure of 363 MPa. The formation of TaB₂/Carbon at TaC grain boundaries helps in pinning the grain boundary and inhibiting grain growth. The effect of B₄C addition on hardness and elastic modulus measured by nanoindentation and the indentation fracture toughness has been studied. Relative fracture toughness increased by up to 93% on B₄C addition.

© 2010 Elsevier B.V. All rights reserved.

1. Introduction

Applications involving temperatures more than 2000 °C such as rocket nozzles, scramjets and supersonic re-entry vehicles require materials with ultra high melting point, high temperature strength and high temperature erosion resistance. Tantalum carbide (TaC) is an interesting compound due to its remarkable high temperature properties. The high hardness (>20 GPa), high melting point (>3800 °C) and resistance to chemical attack and oxidation can be attributed to the presence of strong covalent-metallic bond [1–3]. TaC also possesses good catalytic properties along with good thermal and electrical conductivity [3]. Tantalum carbide (TaC) has the NaCl type structure (B1, space group *Fm* $\bar{3}$ *m*) and can accommodate large vacancies in the carbon lattice, without changing the crystal structure [4]. Tantalum also forms a hexagonal carbide Ta₂C. The ζ -phase having a composition of Ta₄C₃ have been reported in two- and three-phase samples in the Ta–C system between hexagonal TaC_{0.52} and cubic TaC_{0.73} compositional range [5]. The mechanical properties of TaC depend on the C/Ta atomic ratio. The highest fracture toughness of 12.7 ± 0.7 MPa m^{1/2} is reported for TaC_{0.6} and highest hardness value of 20 ± 0.5 GPa for TaC_{0.8} carbides [6].

Tantalum carbide has been difficult to sinter due to its covalent bonding, low self-diffusion coefficient and high activation energy for viscous flow [7,8]. It was reported that even hot pressing at a temperature of 3050 °C at 15.7 MPa produced a density of only 90.5% [7]. Employing smaller particle size for TaC (<0.6 μm) led to a densification of up to 97.5% by pressureless sintering at 2300 °C [9]. Zhang et al. have used C and B₄C as the sintering aid for improving the densification [8]. A relative density of 97% was achieved in hot pressed TaC containing 0.78 wt.% C, at 2300 °C and 30 MPa pressure with a 45 min hold time in helium atmosphere. Addition of 0.36 wt.% B₄C produced a 98% dense TaC sample at a lower temperature of 2200 °C, which shows the efficacy of boron carbide over C, as the sintering aid [8,10]. A recent study has shown that addition of larger amounts of B₄C (1:8 molar ratio ~3.5 wt.% B₄C) to nano-sized TaC powder leads to densification at 1800 °C without any application of pressure [11]. Kim et al. have used a high frequency induction heating sintering (HFHS) apparatus for the fast sintering of fine TaC powders. Sintering of 33 nm grain size TaC powder at 80 MPa pressure took only 3 min to reach 96% theoretical density with temperatures reaching up to 1400 °C [12]. Similar technique has been used by Sciti et al. for the consolidation of TaC–15 vol.% MoSi₂ and TaC–15 vol.% TaSi₂ composites to achieve 96% density within 20 min for temperatures below 1850 °C [13]. Free standing TaC components have also been synthesized using Vacuum Plasma Spray technique [14]. However, the high temperature and low pressure conditions resulted in the partial decomposition of TaC to Ta₂C

* Corresponding author. Tel.: +1 305 348 1701.

E-mail address: agarwala@fiu.edu (A. Agarwal).

and TaC_x ($0.83 \leq x \leq 0.94$). Hot pressing has also been employed to produce TaC reinforced with carbon fibers for space applications [15,16].

In recent years, Spark Plasma Sintering (SPS) also known as Electric Field Assisted Sintering (EFAS) and Field Assisted Sintering Technique (FAST) has been employed several researchers to sinter ultra high temperature ceramics such as HfB_2 , HfC , ZrB_2 , ZrC . The high sintering rates and lower sintering temperature required for SPS are not only advantageous for energy savings, but also result in dense microstructures with decreased grain growth. Groza and Zavaliangos have shown that SPS produces higher densities for given temperature of sintering as compared to liquid phase sintered WC–10 wt.% Co and hot pressed Fe–2 wt.% Al materials [17]. An excellent review of SPS has been provided by Munir et al. [18]. It is believed that sintering is enhanced due to the cleaning action of micro-plasma formed between particles due to arcing [18]; although some studies have questioned the presence of micro-plasma [19]. SPS has been utilized for sintering of multi-phase materials for high temperature applications such as HfB_2 –SiC [20], $MoSi_2$ [21], HfB_2 – $MoSi_2$ and HfC – $MoSi_2$ [22,23], ZrB_2 – $MoSi_2$ [23,24], ZrB_2 –SiC [25–27], and ZrC – $MoSi_2$ [28]. HfC having a melting point above $3900^\circ C$ is found to densify only to 70% when sintered at $1950^\circ C$ for 60 min without application of pressure [29]. However, addition of 5 vol.% of $MoSi_2$ helped in densification up to 98% [29]. Hafnium carbide [22,23] and zirconium carbide [23] powders have been successfully consolidated to 98–99% dense compacts by SPS at 2100 – $2200^\circ C$ at a pressure of 65 MPa and hold time of 3 min. The short sintering times required for SPS is evident from these two studies. However, even the 3 min sintering time was found to increase the mean grain size of ZrC from $\sim 3.8 \mu m$ (starting particle size) to $13 \mu m$, and that of HfC from $0.8 \mu m$ to $19 \mu m$. The addition of $MoSi_2$ in the quantity of 1–9 vol.% leads to a decrease in the sintering temperature to $1750^\circ C$. It was also found that the grain growth was inhibited by addition of $MoSi_2$ and contained to 1–2 μm from HfC – $MoSi_2$ and 4–7 μm for ZrC – $MoSi_2$ materials [23]. $MoSi_2$ reacted with ZrC and HfC leading to the formation of SiC which does not deteriorate the properties of the composite [23]. The low temperature phases like SiC and $MoSi_2$ not only serve as sintering aids but also help in improving the oxidation resistance [27].

The use of SPS for densification of TaC has not received much attention. Even as this article was being prepared, a first report on the use of SPS for densification of TaC was published by Khaleghi et al. [30]. TaC powder of –325 mesh size ($<44 \mu m$) was consolidated using SPS at a low pressure of 30 MPa with temperature being in the range of 1900 – $2400^\circ C$. Sintering at $1900^\circ C$ for 5 min led to densification of 68% while increasing the temperature to $2400^\circ C$ increased the density up to 97%. Addition of 0.77 wt.% carbon nanotubes (CNTs) increased the density of TaC sintered at $2300^\circ C$ from 92% to 96% and the rupture strength from 336 MPa to 550 MPa [30]. The grain size was found to be dependent on the sintering temperature and increased from $0.33 \mu m$ at $1900^\circ C$ to $9.0 \mu m$ at $2400^\circ C$. In the present work, SPS has been carried out on sub-micron size ($0.36 \pm 0.13 \mu m$) TaC powder. Sintering has been carried out at significantly higher pressures, while keeping the temperature lower at $1850^\circ C$, to study the effect of pressure on densification and grain size. Sintering aid like B_4C , have been employed in previous studies had a size of $0.8 \mu m$ as compared to 1–5 μm size of TaC [10]. Thus in this study, the effect of nano-sized B_4C was studied on the densification and grain growth of TaC. The mechanism of sintering is studied using high resolution transmission electron microscopy (HR-TEM). Effect of pressure and nano-sized B_4C addition on the elastic modulus, hardness and relative fracture toughness of TaC is also determined.

2. Experimental

2.1. Powder feedstock and preparation

Tantalum carbide powder was obtained from Inframat Advanced Materials LLC, CT, USA. The specification on the composition by weight was a purity of 99.7% with total carbon $\geq 6.2\%$, free carbon $\leq 0.15\%$, Nb $< 0.3\%$, and O between 0.15 and 0.3%. The mean TaC particle size measured from SEM image shown in Fig. 1a, was $0.36 \pm 0.13 \mu m$. Boron carbide nanopowder was obtained from MTI Corporation, CA, USA. The average particle size was specified as 50 nm and the purity level was 98%. Fig. 1b shows the fine size of the B_4C powders. In order to prepare TaC–1 wt.% B_4C powder, 0.25 g of B_4C powder was ultrasonicated in 50 ml of acetone for

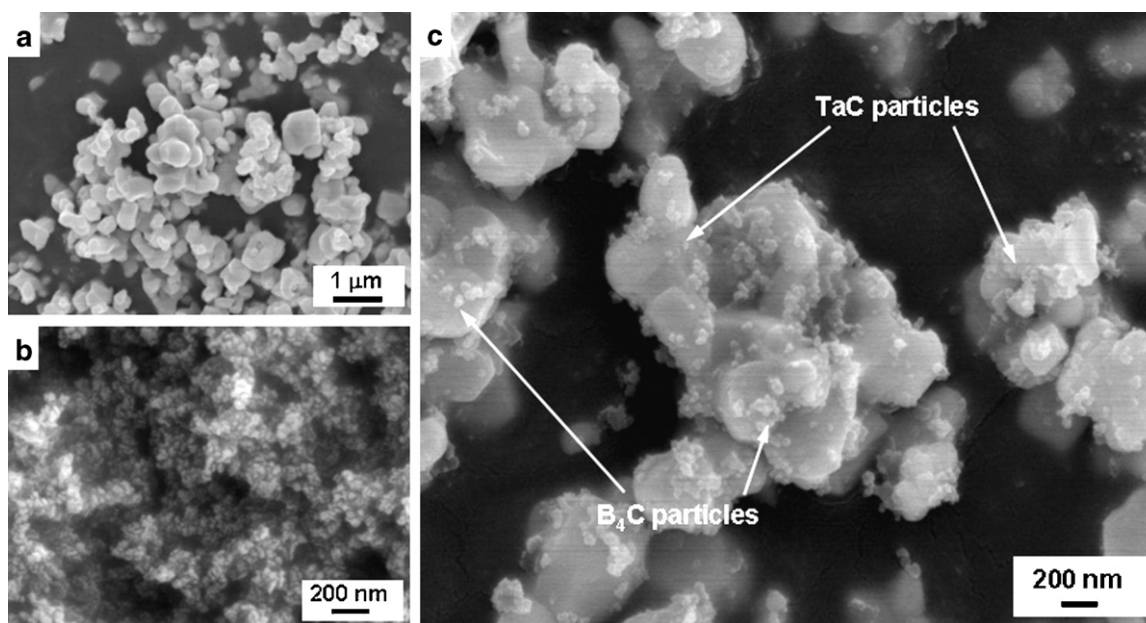


Fig. 1. SEM images showing (a) as-received TaC powders, (b) as-received B_4C nano-powders, and (c) TaC–1 wt.% B_4C powder mixture.

90 min followed by addition of 24.75 g of TaC powder. The mixture was ultrasonicated for 90 more minutes. The mixture was dried at 50 °C. The dried powder was crushed in an Agate mortar and pestle to break the loose agglomerates. Fig. 1c shows the SEM image of TaC–1 wt.% B₄C powder showing homogeneously dispersed nano B₄C on TaC particles.

2.2. Consolidation by spark plasma sintering

Spark plasma sintering (SPS) was utilized to consolidate TaC based powders. SPS was carried out in Argon atmosphere at 1850 °C. The heating rate of 200 °C min⁻¹ was adopted to reach the maximum temperature with a hold time of 10 min. SPS was carried out at three different pressures of 100 MPa, 255 MPa and 363 MPa. The 100 MPa samples were approximately 4–5 mm thick and 20 mm in diameter. The samples sintered at 255 and 363 MPa had a thickness of 2–3 mm and were prepared in a 10 mm diameter silicon carbide die with silicon carbide punches. SPS was carried out at Thermal Technology LLC, CA, USA. Hereafter, the TaC samples prepared at 100, 255 and 363 MPa pressure will be named as TaC-100, TaC-255 and TaC-363 respectively. Similarly, TaC–1 wt.% B₄C samples prepared at 100, 255 and 363 MPa pressure will be named as TaC-BC-100, TaC-BC-255 and TaC-BC-363 respectively.

2.3. Microstructural characterization of the composites

Sintered TaC samples obtained were ground using SiC papers to remove the graphite layer attached on all surfaces. Subsequently, the bulk density was measured using water immersion technique employing the Archimedes principle. The relative density of the TaC samples was calculated as a % of true density, which was measured for the powders using a Helium gas pycnometer (Accupyc 1340, Micromeritics Instrument Corporation, Norcross, GA, USA) to be 14.67 g cm⁻³. The relative density of the TaC-BC samples was calculated as a % of the theoretical density, which was calculated from the rule of mixtures, to be 14.0 g cm⁻³. Metallographic samples were prepared by grinding until 600 grit SiC paper and then polished using diamond suspension till 0.1 μm finish. Fracture surface of the SPS samples were prepared by breaking the samples by hitting with a hammer and observing normal to the fracture surface. A JEOL JSM 630F scanning electron microscope (SEM) with a field emission gun was used to study the morphology of the powders and fracture surfaces. X-ray diffraction was carried out using a Bruker D500 X-ray Diffractometer using Cu-Kα X-rays at a scan rate of 1°/min. A Philips/FEI Tecnai F30 transmission electron microscope (TEM) using a field emission gun and operating at an accelerating voltage of 300 kV was used to study the microstructure.

2.4. Mechanical property characterization

Hardness and elastic modulus of the sintered compacts were measured by nanoindentation on the polished cross section. A

Hysitron Triboindenter (Hysitron Inc., Minneapolis, MN, USA) was used to carry out the tests. Indentations were carried out at a load of 4.5 mN. The load function comprised of loading to 4.5 mN in 10 s followed by holding at maximum load for 2 s and then unloading to zero load in 10 s. The reduced elastic modulus obtained from nanoindentation (E_r) by the Oliver and Pharr method was corrected for the deformation of the indenter, which is significant due to the high elastic modulus/hardness of the samples, using the following equation.

$$\frac{1}{E_r} = \frac{1 - \nu_s^2}{E_s} + \frac{1 - \nu_i^2}{E_i} \quad (1)$$

Here, E_s is the actual elastic modulus of the sample, and ν_s is the Poisson's ratio of TaC which is taken equal to 0.24 [31], E_i and ν_i are the elastic modulus and Poisson's ratio of the indenter which is taken equal to 1141 GPa and 0.07 [32] respectively. Two 5 × 5 indentation test matrices (50 indents) were made at different locations on each of the samples with 9 μm spacing between each indentation. Fracture toughness was evaluated using a Vickers indenter on the polished cross section using a microhardness tester (Shanghai Taiming Optical Instrument Co. Ltd., model HXD-1000 TMC, Shanghai, China) at a load of 500 g and dwell time of 15 s. The crack lengths (c) were measured from the center of the indents and the fracture toughness K_{IC} was computed using the Anstis equation [33]:

$$K_{IC} = 0.016 \left(\frac{E}{H} \right)^{1/2} \frac{P}{c^{3/2}} \quad (2)$$

where E is the elastic modulus, H is the hardness and P is the load applied (500 g).

3. Results and discussion

3.1. Density and microstructure of the sintered TaC compacts

Table 1 lists the relative and true density of the SPS compacts. Fig. 2 shows the variation of the relative density of the compacts with the pressure. The density increases with the pressure and a 100% density was achieved for 255 MPa and higher pressure for TaC. For the sake of comparison, TaC was also consolidated by SPS at 1800 °C and 2200 °C at low pressure of 60 MPa with a 5 min hold time. Both samples had a very low density of 86% indicating that temperature had little effect on the density. Fig. 3 shows the SEM micrographs of the fracture surface of these samples. The pores between the particles can be clearly seen. Fig. 3b shows that the sample synthesized at 2200 °C/60 MPa has large pores (5–10 μm) between severely coarsened TaC particles. Khaleghi et al. recently reported the relative density of TaC sample prepared by SPS (hold time = 5 min) at a pressure of 30 MPa and temperature of 1900 °C and 2300 °C to be 68% and 83% respectively [30]. The higher densification (86%) seen in our study at 1800 °C could be due to sub-micron TaC particles as well as increased pressure of 60 MPa. Liu et al.

Table 1
Properties of TaC and TaC–1 wt.% B₄C compacts prepared by SPS.

Powder	SPS compact	Density (g cm ⁻³)		Grain size (μm)	Nano-hardness (GPa)	Elastic modulus (GPa)	Relative fracture toughness
		Actual	Relative (%)				
TaC	TaC-100	13.0	89	0.56 ± 0.12	17.8 ± 3.2	335 ± 28	^a
	TaC-255	14.6	100	4.93 ± 1.99	26.3 ± 2.7	469 ± 46	1 ± 0.07 ^b
	TaC-363	14.6	100	5.6 ± 2.4	25.7 ± 5.7	457 ± 39	0.99 ± 0.09
TaC–1 wt.% B ₄ C	TaC-BC-100	13.6	97	1.18 ± 0.39	21.6 ± 1.8	403 ± 19	^a
	TaC-BC-255	14.2	101	0.71 ± 0.26	24.6 ± 2.2	364 ± 38	1.34 ± 0.22
	TaC-BC-363	14.4	103	1.0 ± 0.29	23.4 ± 1.5	510 ± 15	1.93 ± 0.14

^a Indentation fracture toughness was not measured due to porous nature of the compact.

^b Fracture toughness of TaC-BC-255 was taken as the reference for normalizing indentation toughness values.

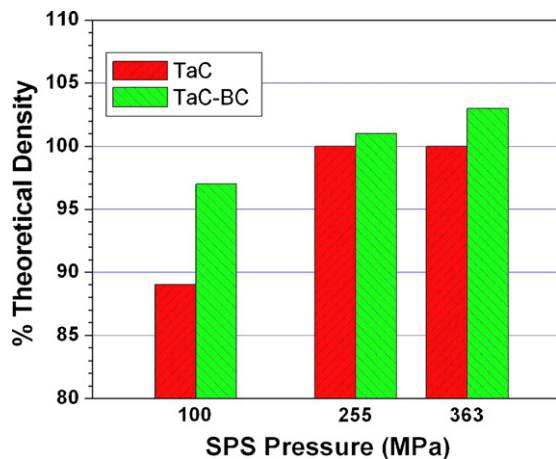


Fig. 2. Variation of % theoretical density of sintered TaC and TaC-B₄C with SPS pressure.

have obtained a density of 95% by using fine powders (<0.6 μm) by pressureless sintering at 2200 °C for 30 min [9] indicating the finer particle sizes aid in lowering the sintering temperature. Zhang et al. reported a density of 75.2% and 89.1% in hot pressed samples (45 min hold time) at a pressure of 30 MPa and temperatures of 1900 °C and 2200 °C respectively [8]. It is to be kept in mind that in hot pressing or pressureless sintering methods, the heating rates are usually low, e.g. 5–50 °C/min whereas SPS employs very high heating rates (150–300 °C/min) and short sintering times resulting in faster densification with retention of fine grain size. As seen from

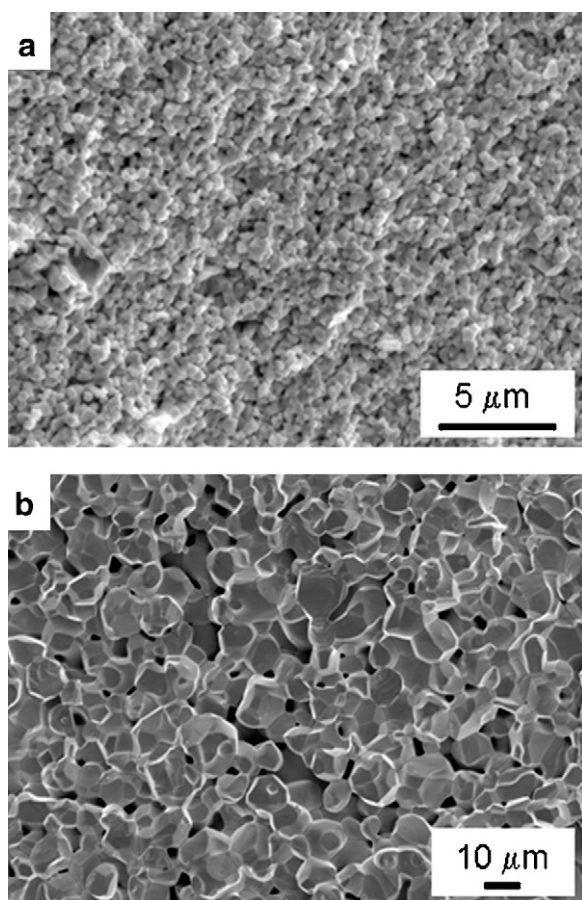


Fig. 3. SEM micrographs of the fracture surfaces of TaC samples prepared by SPS at a pressure of 60 MPa and (a) 1800 °C, and (b) 2200 °C.

Table 1, the density of TaC sintered at 1850 °C with a pressure of 100 MPa and 10 min hold time was 89%. Khaleghi et al. obtained a density of 92% for TaC samples prepared by SPS at 2300 °C, 30 MPa and 20 min hold time [30]. The present study and Ref. [30] indicate that pressure has a significant effect on the density obtained during SPS.

Munir et al. have expressed the pressure dependency of densification rate by the following relation [18]:

$$\frac{d\rho}{(1-\rho)dt} = B \left(g \frac{y}{x} + P \right) \quad (3)$$

Here ρ is the density expressed as a fraction of theoretical value, B is a term that includes diffusion coefficient (dependent on temperature), g is a geometric constant, y is the surface energy term, x is length scale parameter related to particle size, t is time of sintering, and P is the applied external pressure. It is well known that diffusion coefficient increases with the temperature in accordance with an Arrhenius type of equation. However, pressure has an opposite effect on the diffusion coefficient. Diffusion coefficient is related to the pressure by the following relation [34]:

$$\left[\frac{\partial \ln D}{\partial P} \right]_T = - \frac{\Delta V}{kT} \quad (4)$$

where D is the diffusion coefficient, P is the pressure, ΔV is the activation volume for diffusion and T is the absolute temperature. Since the activation volume for diffusion of a species is always positive, it follows that the increase in pressure reduces the diffusion coefficient of the species. In this study, the TaC sample sintered at 2200 °C/60 MPa was found to be low (86%) density compared to the TaC sample sintered at 1850 °C/100 MPa (89%) indicating that pressure has a significant effect, i.e. the second term on the right hand side of Eq. (3) has a dominating effect on densification. Table 1 shows that 100% theoretical density was achieved at a pressure of 255 MPa for TaC. The addition of 1 wt.% nano-sized B₄C improved the density of TaC-100 from 89% to 97%. Similar improvement of density from 94% to >98% was reported for TaC samples hot pressed at 2300 °C by addition of 1 wt.% B₄C [10]. Although TaC-BC-255 sample had a density value which was 101% the estimated value, it had some localized porosity, which seemed to be regions of higher nano-B₄C content which consolidated faster and the higher shrinkage resulted in the pores. TaC-BC-363 showed fully dense structure with a measure density equal to 103% of the estimated true density. The reason for observed densities being more than the true density is the reaction between B₄C and TaC leading to formation of new products which is discussed in Section 3.2.1. These new products are expected to alter the true density for 100% dense sample. However, the change is expected to be less because of the small amount of reaction products.

Fig. 4 shows the fracture surface of sintered TaC compacts. TaC-255 and TaC-363 samples do not show any pores, while small pores are seen in TaC-100. The fracture is mostly inter-granular in nature showing the faceted morphology of the grains. A few of the grains have also fractured from the middle as indicated by the flat surface of the grain indicating a brittle cleavage fracture. Fig. 5 shows the fracture surfaces of TaC-BC samples. The fracture surface morphology of TaC-BC samples is distinctly different than TaC samples. The grains have an elongated morphology in the TaC-BC samples as compared to equi-axed morphology in TaC samples. Fig. 6 shows a comparison of high magnification SEM images of TaC-363 and TaC-BC-363 samples. In some regions in TaC-363, abnormal grain growth was observed. This is visible from the large grains which have grown at the expense of smaller grains as seen in Fig. 6a. This phenomenon was not observed in samples prepared at 100 and 255 MPa pressure. Flat cleavage fracture of grains was observed in the TaC-363 sample indicating that the strength of the grain

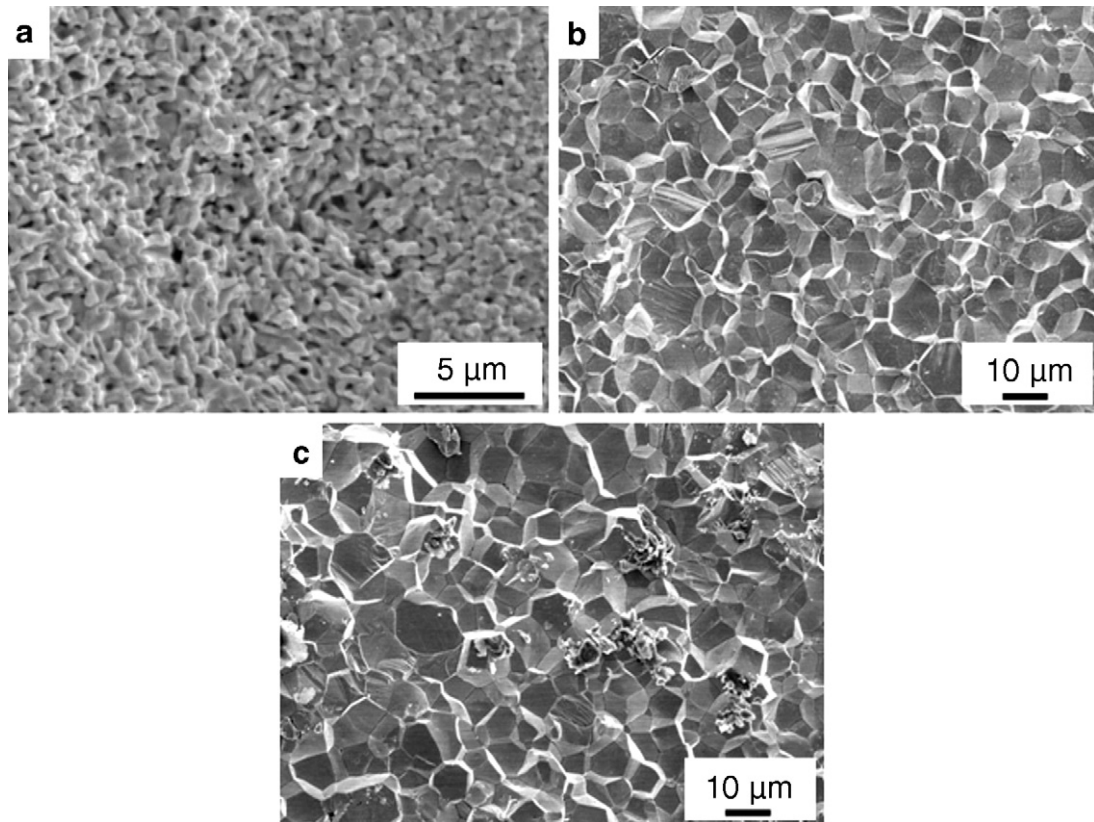


Fig. 4. SEM micrographs of fracture surfaces of TaC samples prepared by SPS at (a) 1850 °C and 100 MPa, (b) 1850 °C and 255 MPa, and (c) 1850 °C and 363 MPa.

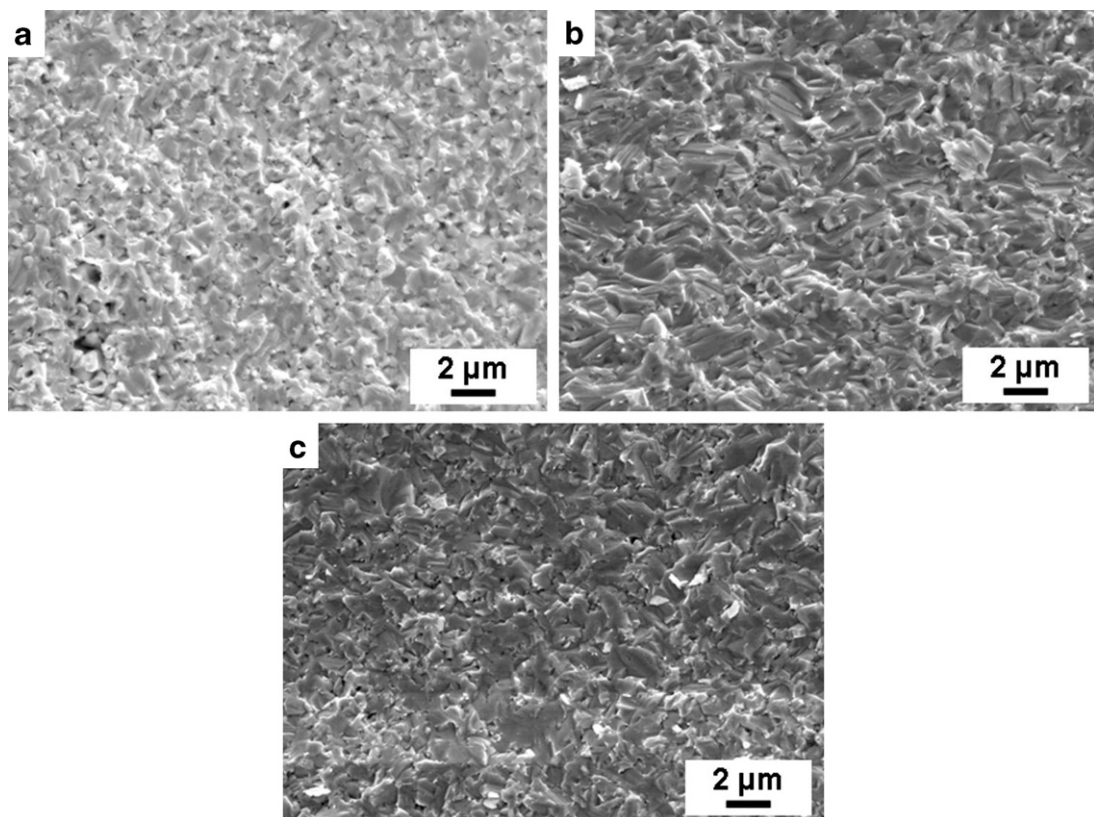


Fig. 5. SEM micrographs of the fracture surface of (a) TaC-BC-100, (b) TaC-BC-255 and (c) TaC-BC-363 samples.

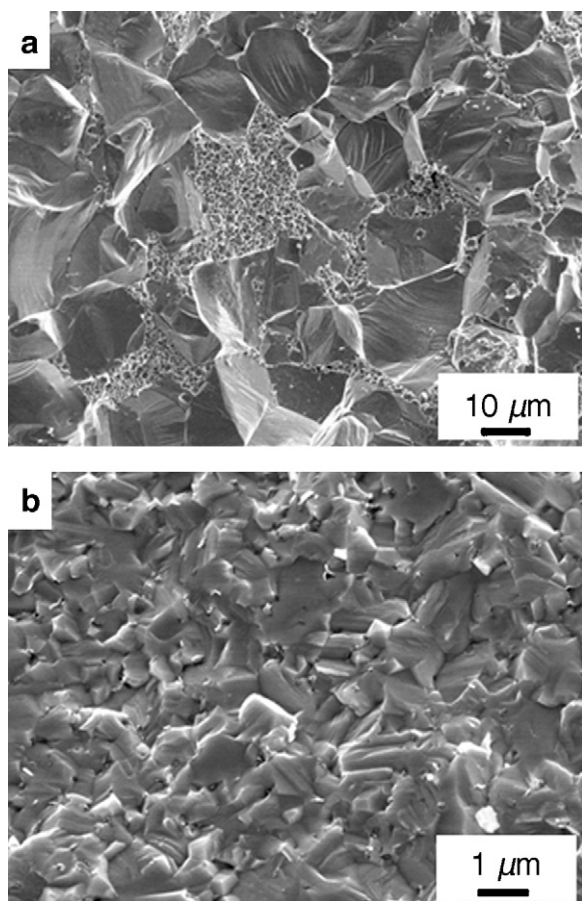


Fig. 6. High magnification SEM micrographs of fracture surface of (a) TaC-363, and (b) TaC-BC-363 samples.

boundaries increased with the SPS pressure indicating better consolidation. Fig. 6b indicates a slightly fibrous fracture surface for TaC-BC-363 suggesting that grains have undergone some degree of localized plastic deformation before fracturing. This could be due to the formation of carbon (explained in Section 3.2.1), which could lead to some deformation before fracture due to its softer nature.

3.2. Effect of SPS pressure and B_4C addition on the grain size

It can be seen from Figs. 3–5, that the grain size of sintered TaC and TaC-BC compacts is different from the starting powder. The grain size was measured from several SEM images at different magnifications. Only those particles were taken into consideration which seemed to have more than half of them visible on the fracture surface. The average of at least 50 such particles was taken as the measure of the average grain size which is listed in Table 1. Fig. 7 shows the variation of TaC grain size with SPS pressure. It is observed that with an increase in SPS pressure, grain size of TaC increases. The grain size of TaC-100 sample is $0.56 \pm 0.12 \mu\text{m}$ which is closer to the starting particle size ($0.36 \pm 0.13 \mu\text{m}$). The grain size of the samples synthesized at 1800°C and 2200°C at 60 MPa pressure was $0.33 \pm 0.08 \mu\text{m}$ and $8.36 \pm 2.95 \mu\text{m}$ respectively indicating that grain size is very sensitive to SPS temperature, while densification is not. Grain size has been found to increase with SPS temperature in other materials such as hydroxyapatite [35]. At the SPS temperature of 1850°C , the grain size was found to increase with SPS pressure. This is contrary to the reports in the literature where the grain size has been observed to reduce as in case of cubic zirconia with increase in SPS pressure [18]. Grasso et al. have also reported decrease in the grain size of spark plasma sin-

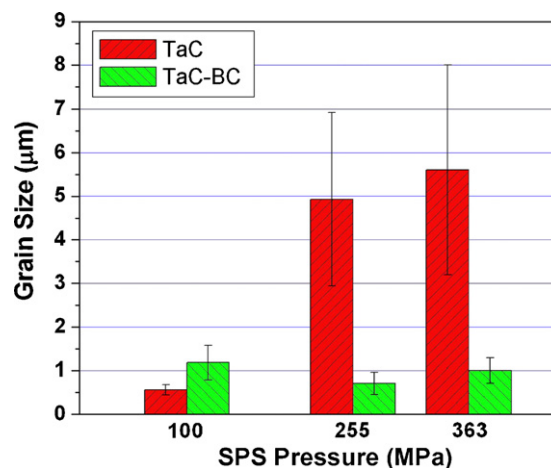


Fig. 7. Variation of grain size of sintered TaC and TaC-BC compacts with SPS pressure.

tered tungsten carbide with increasing pressure from 5 to 80 MPa and even observed abnormal grain growth at 5 MPa pressure [36]. However, our observations for TaC are contradictory as grain size of TaC increases with increasing SPS pressure, as seen in Fig. 7. Increased pressure has an effect of decreasing the diffusion coefficient according to Eq. (4) and hence is expected to slow down diffusion related processes like grain growth. It is observed from Figs. 4 and 5 that the 255 MPa and 363 MPa sintered samples are 100% dense without any porosity. Thus the grain growth is not expected to be hindered due to pore-pinning which limits the grain size. The pressures employed in this study are significantly higher than that observed in the literature. So, the plausible reasons for increasing grain size with SPS pressure is that such grain growth may occur due to the increased heat transfer at such higher pressures and movement of interfaces under the applied pressure due to a creep kind of phenomena. The study of the mechanism of the sintering and grain growth will require additional experiments at different pressures as well as hold times, which is beyond the scope of the present study.

The TaC-BC-100 sample shows slightly higher grain size than TaC-100 sample. This is because the TaC-100 sample has densified only to 89% and hence grain growth stage has not been attained. This is supported by the fact that the measured grain size of TaC-100 sample was very close to original particle size. Addition of B_4C has accelerated the densification to 97% and the grain growth stage seems to have just begun. As seen from Figs. 4 and 6, the grain size of TaC-BC-255 and TaC-BC-363 are smaller compared to the corresponding TaC samples indicating that addition of B_4C acts as a grain growth inhibitor at higher sintering pressures. Thus, addition of B_4C has an added advantage. This is contradictory to the observation of Zhang et al. who have reported an increase in the grain size for hot pressed TaC-0.36 wt.% B_4C prepared at 2200°C and 2300°C [8]. There could be two reasons for this. One is that the temperatures were quite high (2200 – 2300°C compared to 1850°C in our case) and pressures were lower (30 MPa compared to 100–363 MPa in our case) which would lead to increase in diffusivities leading to higher grain growth rates. Moreover, the nano-sized B_4C utilized in this study was dispersed very uniformly (Fig. 1c) and was effective in pinning the TaC boundaries on all sides. The sintering mechanism and grain growth inhibition was further studied with the help of high resolution TEM as described in the following section.

3.2.1. Mechanism of sintering with nano- B_4C addition

The addition of B_4C has dual advantages viz. (i) as a sintering aid and (ii) grain growth inhibitor. It has been reported that TaC

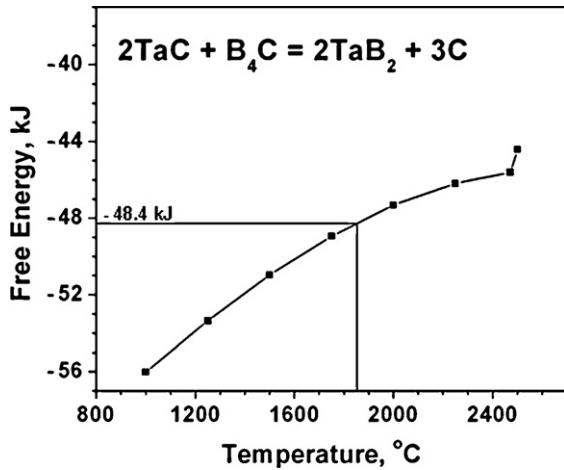


Fig. 8. Variation of Free energy of TaB₂ formation by reaction between TaC and B₄C as a function of temperature.

reacts with B₄C resulting in formation of TaB₂ [8,10] according to the following reaction:

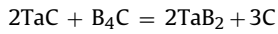


Fig. 8 shows the free energy of the reaction as a function of temperature as calculated from Thermochemical database of software

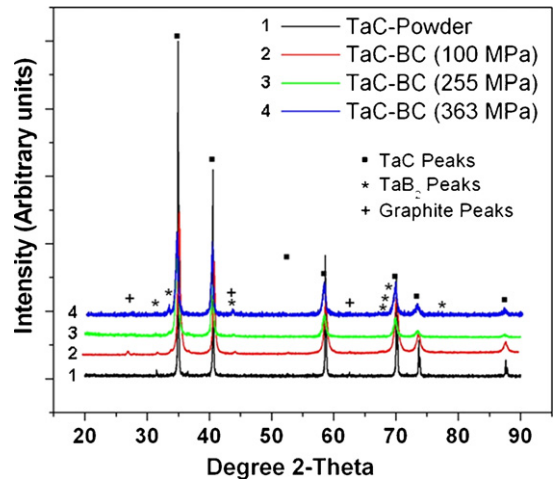


Fig. 9. XRD patterns of TaC-BC samples synthesized at 1850 °C and different pressures indicating formation of TaB₂.

FactSage [37]. It is observed that the free energy of the reaction is negative ($-48.4 \text{ kJ mol}^{-1}$) at the SPS temperatures of 1850 °C. Also the heat of reaction was found to be equal to $-62.3 \text{ kJ mol}^{-1}$ at 1850 °C. This indicates that not only the reaction is thermodynamically feasible but is also exothermic and will help in further consolidation. The large surface area and good dispersion of nano-

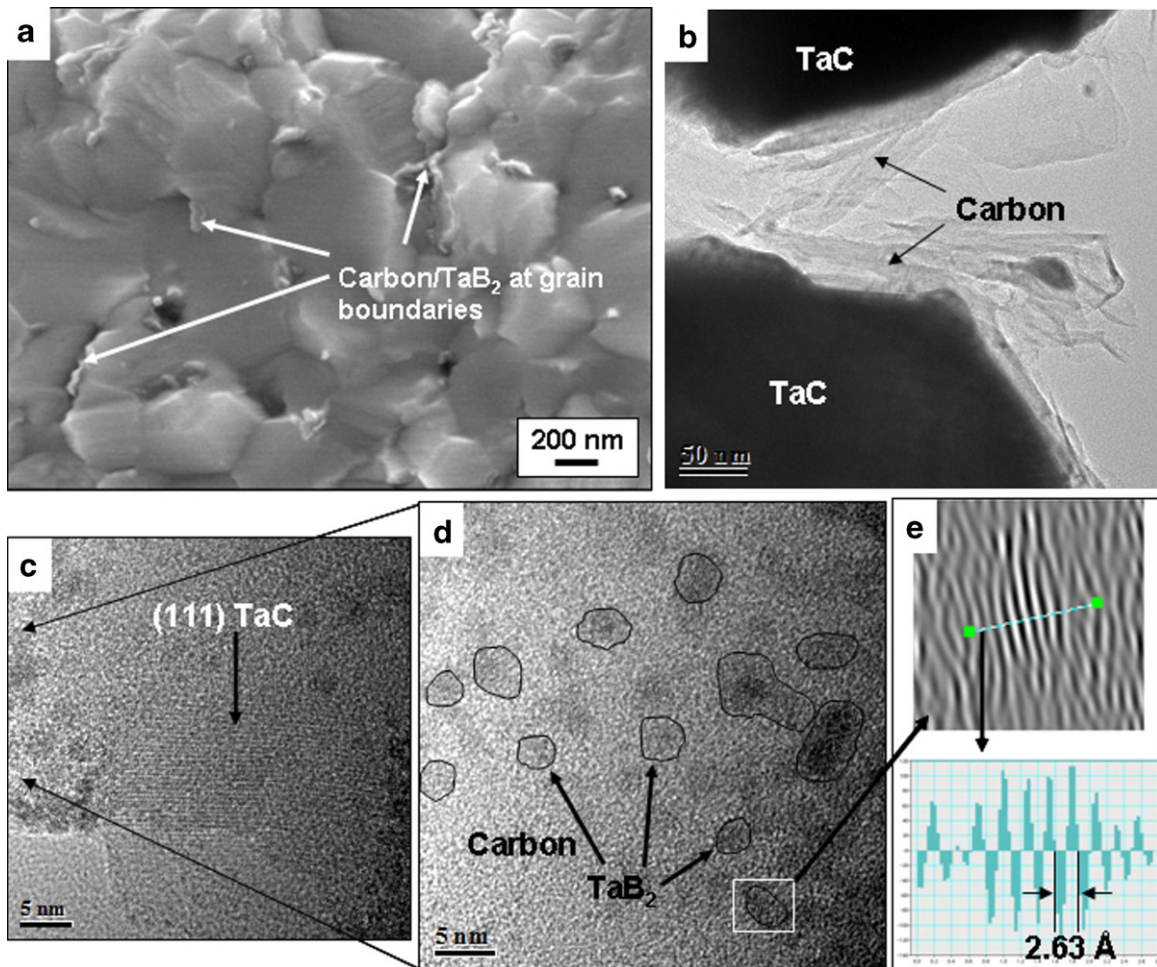


Fig. 10. (a) SEM micrograph of the fracture surface of TaC-BC-363 sample indicating the presence of Carbon/TaB₂ at TaC grain boundaries, (b) TEM image of TaC-BC-363 sample showing the presence of carbon flakes between TaC grains, (c) high resolution image showing the (1 1 1) planes of TaC and amorphous carbon containing islands of crystalline phase, (d) high resolution TEM image showing the lattice fringes of crystalline phase, and (e) the inverse FFT image showing inter-planar spacing corresponding to (10 $\bar{1}$ 0) TaB₂.

B₄C powder (Fig. 1c) further facilitates sintering process. Talmy et al. have reported that fine size TaC powders can be pressureless sintered at 1800 °C using 2 wt.% carbon black as sintering aid [11]. Zhang et al. have also reported increase in the density of TaC by addition of 0.78 wt.% C synthesized by hot pressing [8]. Carbon concentration in TaC-363 and TaC-BC-363 samples was measured by LECO combustion analysis and found to be 6.19 wt.% and 6.42 wt.% respectively. Thus, the formation of extra carbon may also assist sintering. Fig. 9 shows the XRD patterns of the TaC-BC samples indicating the formation of TaB₂ and carbon traces. TaB₂ has been reported to have Young's modulus of 551 ± 8 GPa, Vickers hardness of 25.6 ± 0.7 GPa and a fracture toughness of 4.5 ± 0.3 MPa m^{1/2} and a melting temperature of 3200 °C [38]. Zhang et al. have reported an increase in density of hot pressed TaC samples from 94% to 98.6% by addition of 10 wt.% TaB₂, while the elastic modulus was enhanced from 472 ± 7 GPa to 543 ± 7 GPa without affecting the fracture toughness [39]. Therefore, it is expected that the formation of TaB₂ will not deteriorate the properties of TaC compacts.

Fig. 10a shows the SEM image of the fracture surface of TaC-363. It can be seen that there are phases present at the grain boundaries of TaC which could be Carbon/TaB₂ phase mixtures. Fig. 10b shows a TEM image of TaC-BC-363 showing the presence of flaky carbon like material between TaC grains. Fig. 10c shows a high resolution TEM image showing (1 1 1) TaC surrounded by some amorphous phase containing crystalline islands. The lattice fringe images of the crystalline islands observed in the high resolution image of Fig. 10d were refined by obtaining the Fourier transform, refinement of the diffraction spot pattern, followed by Inverse FFT operation to generate the image shown in Fig. 10e. The crystalline islands were found to have a plane spacing of 2.63 Å which correspond to (1 0 1̄ 0) planes of TaB₂ which have a plane spacing of 2.683 Å. The measured value of 2.63 Å suggests a 2% compressive strain in the TaB₂ lattice. This could be due to the fact that the carbon formed due to the reaction has a low density and the volume increase would result in compressive stress in the entrapped TaB₂ particles due to constrain of TaC grains. The presence of TaB₂ peaks in the X-ray diffraction pattern of TaC-BC samples also supports TaB₂ phase formation.

3.3. Mechanical properties of TaC and TaC-BC compacts

Fig. 11 shows the nano-hardness and elastic modulus values of TaC and TaC-BC samples synthesized at different SPS pressures. The scatter in the data is attributable to the localized nature of the nanoindentation testing which results in values which are sensitive to the local microstructure. However, the average value is an indication of the relative mechanical properties of the TaC and TaC-BC samples. The increased hardness of TaC for TaC-255 and TaC-363 sample as compared to TaC-100 sample can be attributed to the increased density. It is also observed that addition of B₄C leads to increase in the hardness for the 100 MPa sample. This can be attributed to the increased density by addition of B₄C. The hardness of TaC-255 and TaC-363 sample was higher than the corresponding TaC-BC sample. This could be due to the fact that the carbon generated due to reaction between B₄C and TaC will tend to soften the compact. Fig. 11b indicates that the elastic modulus of TaC increases with an increase in SPS pressure. This is again due to the increase in density of the compacts. The elastic modulus of TaC-255 and TaC-363 are similar due to similar densities. It is observed that addition of B₄C leads to increase in elastic modulus for samples synthesized at 100 and 363 MPa. The porosity present in the TaC-BC-255 sample along with the formation of carbon by the reaction might be leading to reduced elastic modulus at 255 MPa pressure as compared to the TaC-255 sample. The scatter in the data represents the localized nature of the nanoindentation tests and its sensitivity to the local microstructure in the test area. Recently a novel method

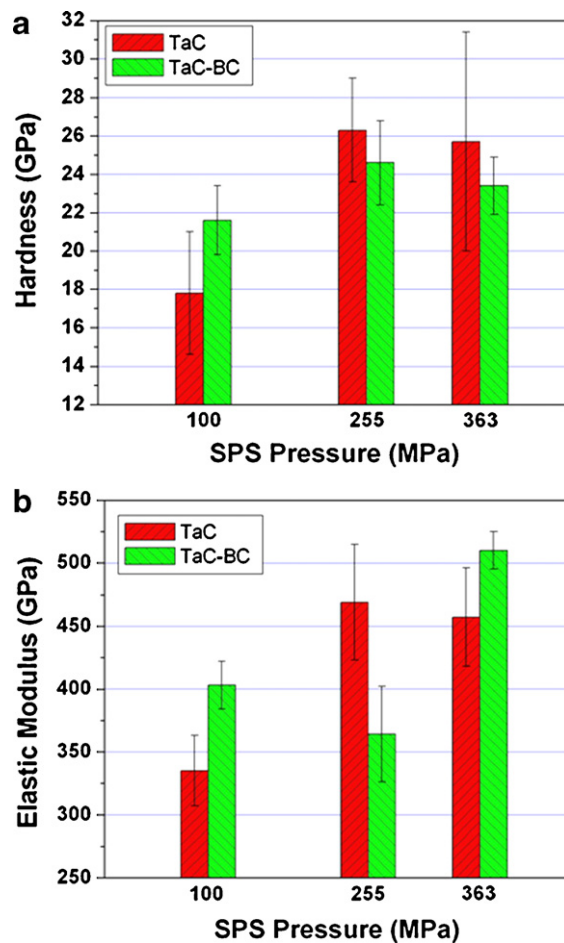


Fig. 11. Variation of (a) nanohardness and (b) elastic modulus of sintered TaC and TaC-BC samples with the SPS pressure.

for measuring the transverse rupture strength of the ceramic disks prepared by SPS has been reported [30]. This method is unique as it prevents crack generation in ceramic during machining of rectangular flexure samples from disks. The bulk TaC properties and the factors affecting them are the focus of our future studies.

Fig. 12 shows the relative fracture toughness of the samples synthesized at 255 and 363 MPa. The values were normalized with the fracture toughness for TaC-255 sample in order to see the relative

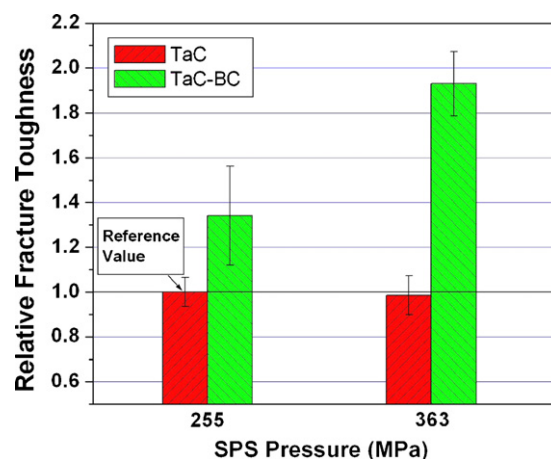


Fig. 12. Relative fracture toughness of sintered TaC and TaC-BC samples with SPS pressure normalized to the value of TaC-255 sample.

improvement. Fracture toughness was not measured for the samples synthesized at 100 MPa due to higher porosity content in these samples. It is known that the accuracy of fracture toughness values measured by indentation is debatable for porous samples [40]. However, a relative enhancement in the toughness property can be gauged due to changes in processing or chemistry of the materials by using the indentation toughness values. Thus in Fig. 12, the values of indentation toughness are represented by normalizing the values with respect to TaC-255 sample. It is observed that the fracture toughness remains same for TaC-255 and TaC-363 samples due to the similar densities and chemistry. With the addition of B₄C, the fracture toughness is found to increase. An increase in the toughness up to 93% was observed for TaC-BC-363 as compared to TaC-363. As observed in Fig. 6b, fracture surface of TaC-BC-363 sample showed some signs of localized plastic deformation. The energy dissipation during this deformation might be the reason for increased toughness of the TaC-BC composites. Another reason for increased toughness could be the presence of carbon and nanosized TaB₂ at the TaC boundaries which can increase the fracture energy. The decreased grain size is also expected to improve toughness by frequent crack deflections as it propagates along grain boundaries.

4. Conclusions

TaC and TaC–1 wt.% B₄C compacts were successfully synthesized to 100% density using spark plasma sintering. The grain-size of TaC samples was found to increase with increasing SPS pressure. Full density was achieved at an SPS pressure of 255 MPa at 1850 °C. It is observed that pressure has a more dominating effect as compared to temperature on densification of TaC. Grain growth was more sensitive to SPS temperature. Nano-sized B₄C was found to act as a sintering aid and a grain growth inhibitor. XRD patterns and TEM images suggested that TaC reacted with B₄C leading to formation of TaB₂ and carbon. The TaB₂/carbon present at grain boundaries leads to pinning of the grain boundaries and arrests grain growth. Hardness and elastic modulus were found to increase with B₄C addition. The relative fracture toughness of the B₄C containing TaC was up to 93% higher than TaC synthesized at 363 MPa pressure.

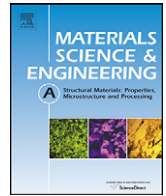
Acknowledgements

The authors acknowledge financial support from US Air Force Office of Scientific Research Grant (Grant No. FA9550-09-1-0297) and thank Program Officer Dr. Joan Fuller. Dr. Daniela Fredrick's assistance with SPS processing at Thermal Technologies is greatly acknowledged. Authors are also thankful to AMERI at FIU for pro-

viding the research facilities and especially to Mr. Neal Ricks and Dr. Y. Liu for their assistance.

References

- [1] Y.J. Chen, J.B. Li, H.Z. Zhai, *J. Cryst. Growth* 224 (2001) 244–250.
- [2] O. Khyzhun, *J. Alloys Compd.* 259 (1997) 47–58.
- [3] J.G. Choi, *Appl. Catal. A* 184 (1999) 189–201.
- [4] R.W. Bartlett, C.W. Smith, *J. Appl. Phys.* 38 (1967) 5428–5429.
- [5] A.I. Gusev, A.S. Kurlov, V.N. Lipatnikov, *J. Solid State Chem.* 180 (2007) 3234–3246.
- [6] K. Hackett, S. Verhoef, R.A. Cutler, D.K. Shetty, *J. Am. Ceram. Soc.* 92 (2009) 2404–2407.
- [7] G.V. Samonov, R.Ya. Petrikina, *Phys. Sintering* 2 (1970) 1–20.
- [8] X. Zhang, G.E. Hilmas, W.G. Fahrenholtz, *J. Am. Ceram. Soc.* 90 (2007) 393–401.
- [9] J.-X. Liu, Y.-M. Kan, G.-J. Zhang, *J. Am. Ceram. Soc.* 93 (2010) 370–373.
- [10] X. Zhang, G.E. Hilmas, W.G. Fahrenholtz, *Mater. Sci. Eng. A* 501 (2009) 37–43.
- [11] I.G. Talmy, J.A. Zaykoski, M.M. Opeka, *J. Eur. Ceram. Soc.* 30 (2010) 2253–2263.
- [12] B.-R. Kim, K.-D. Woo, J.-M. Doh, J.-K. Yoon, I.-J. Shon, *Ceram. Int.* 35 (2009) 3395–3400.
- [13] D. Sciti, L. Silvestroni, S. Guicciardi, D.D. Fabbri, A. Bellosi, *J. Mater. Res.* 24 (2009) 2056–2065.
- [14] K. Balani, G. Gonzalez, A. Agarwal, R. Hickman, S. O'Dell, *J. Am. Ceram. Soc.* 89 (2006) 1419–1425.
- [15] R.E. Riley, T.C. Wallace Sr., US Patent 4,180,428 (1979).
- [16] J.O. Gibson, M.G. Gibson, US Patent 4,278,729 (1981).
- [17] J.R. Groza, A. Zavaliangos, *Mater. Sci. Eng. A* 287 (2000) 171–177.
- [18] Z.A. Munir, U. Anselmi-Tamburini, M. Ohyanagi, *J. Mater. Sci.* 41 (2006) 763–777.
- [19] D.M. Hulbert, A. Anders, J. Andersson, E.J. Lavernia, A.K. Mukherjee, *Scripta Mater.* 60 (2009) 835–838.
- [20] F. Monteverde, *J. Alloys Compd.* 428 (2007) 197–205.
- [21] G. Cabouro, S. Chevalier, E. Gaffet, Y. Grin, F. Bernard, *J. Alloys Compd.* 465 (2008) 344–355.
- [22] D. Sciti, S. Guicciardi, *J. Am. Ceram. Soc.* 91 (2008) 1433–1440.
- [23] D. Sciti, M. Nygren, *J. Mater. Sci.* 43 (2008) 6414–6421.
- [24] A. Balbo, D. Sciti, *Mater. Sci. Eng. A* 475 (2008) 108–112.
- [25] X. Zhang, L. Xu, S. Du, C. Liu, J. Han, W. Han, *J. Alloys Compd.* 466 (2008) 241–245.
- [26] F. Monteverde, A. Bellosi, L. Scatteia, *Mater. Sci. Eng. A* 485 (2008) 415–421.
- [27] S.-Q. Guo, *J. Eur. Ceram. Soc.* 29 (2009) 995–1011.
- [28] D. Sciti, S. Guicciardi, M. Nygren, *Scripta Mater.* 59 (2008) 638–641.
- [29] D. Sciti, L. Silvestroni, A. Bellosi, *J. Am. Ceram. Soc.* 89 (2006) 2668–2670.
- [30] E. Khaleghi, Y.-S. Lin, M.A. Meyers, E.A. Olevsky, *Scripta Mater.* (2010), doi:10.1016/j.scriptamat.2010.06.006.
- [31] L. Lopez-de-la-Torre, B. Winkler, J. Schreuer, K. Knorr, M. Avalos-Borja, *Solid State Commun.* 134 (2005) 245–250.
- [32] K. Park, S. Mishra, G. Lewis, J. Losby, Z. Fan, J.B. Park, *Biomaterials* 25 (2004) 2427–2436.
- [33] G.R. Anstis, P. Chantikul, B.R. Lawn, D.B. Marshall, *J. Am. Ceram. Soc.* 64 (1981) 533–538.
- [34] S.C. Liao, W.E. Mayo, K.D. Pae, *Acta Mater.* 45 (1997) 4027–4040.
- [35] Y.W. Gu, N.H. Loh, K.A. Khor, S.B. Tor, P. Cheang, *Biomaterials* 23 (2002) 37–43.
- [36] S. Grasso, Y. Sakka, G. Maizza, C. Hu, *J. Am. Ceram. Soc.* 92 (2009) 2418–2421.
- [37] C.W. Bale, P. Chartrand, S.A. Degterov, G. Eriksson, K. Hack, R.B. Mahfoud, J. Melançon, A.D. Pelton, S. Petersen, *Calphad* 26 (2002) 189–228.
- [38] X. Zhang, G.E. Hilmas, W.G. Fahrenholtz, *Mater. Lett.* 62 (2008) 4251–4253.
- [39] X. Zhang, G.E. Hilmas, W.G. Fahrenholtz, *J. Am. Ceram. Soc.* 91 (2008) 4129–4132.
- [40] X. Wang, N.P. Padture, H. Tanaka, *Nat. Mater.* 3 (2004) 539–544.



Spark plasma sintered tantalum carbide–carbon nanotube composite: Effect of pressure, carbon nanotube length and dispersion technique on microstructure and mechanical properties

Srinivasa R. Bakshi^a, Vishal Musaramthota^a, David A. Virzi^a, Anup K. Keshri^a, Debrupa Lahiri^a, Virendra Singh^b, Sudipta Seal^b, Arvind Agarwal^{a,*}

^a Plasma Forming Laboratory, Nanomechanics and Nanotribology Laboratory, Department of Mechanical and Materials Engineering, Florida International University, Miami, FL 33174, USA

^b AMPAC and Nanoscience Technology Center, University of Central Florida, Orlando, FL 33816, USA

ARTICLE INFO

Article history:

Received 11 October 2010

Received in revised form

23 November 2010

Accepted 3 December 2010

Available online 10 December 2010

Keywords:

Tantalum carbide

Carbon nanotubes

Spark plasma sintering

Grain growth

Densification

ABSTRACT

TaC–4 wt.% CNT composites were synthesized using spark plasma sintering. Two kinds of CNTs, having long (10–20 μm) and short (1–3 μm) length, were dispersed by wet chemistry and spray drying techniques respectively. Spark plasma sintering was carried out at 1850 °C at pressures of 100, 255 and 363 MPa. Addition of CNTs leads to an increase in the density of 100 MPa sample from 89% to 95%. Short CNTs are more effective in increasing the density of the composites whereas long CNTs are more effective grain growth inhibitors. The longer CNTs are more effective in increasing the fracture toughness and an increase up to 60% was observed for 363 MPa sample. Hardness and elastic modulus are found to increase by 22% and 18% respectively for 100 MPa samples by addition of long CNTs. Raman spectroscopy, SEM and TEM images indicated that the CNTs were getting transformed into flaky graphitic structures at pressure higher than 100 MPa.

© 2010 Elsevier B.V. All rights reserved.

1. Introduction

The borides and carbides of group IV–V metals such as zirconium, hafnium, and tantalum have high hardness, high melting points and good corrosion resistance. These compounds and their composites are particularly suitable for ultra-high temperature applications such as rocket nozzle throat liners, nose and edge components of re-entry vehicles, jet components and protection of carbon–carbon composites [1–6]. Properties such as high temperature stability, high temperature oxidation resistance, thermal shock resistance and high thermal conductivity are desirable for such applications. Pressure-less sintering [7–10], hot pressing [2,11–18], reactive hot pressing [19–21] and plasma spraying [22,23] have been utilized for the fabrication of monolithic or composite structures and coatings of these ultra high temperature ceramics (UHTCs). Spark plasma sintering is a relatively novel consolidation method that has the advantage of short sintering duration and has shown better densification and properties than hot pressing [24]. SPS has been extensively used for synthesis of UHTCs and their composites [11,14,17,25–29].

Tantalum carbide has high melting point of 3880 °C and is stable for a large range of C/Ta ratio of 0.76–1 [13]. The strong covalent–ionic bond results in high hardness of >20 GPa and elastic modulus of up to 550 GPa [30] which makes it extremely suitable for rocket components involving combustion temperatures up to 3500 K. TaC has been consolidated using techniques such as pressureless sintering [7,31], hot pressing [13,15,16,18,32], high frequency induction heating [33,34], vacuum plasma spraying [22] and spark plasma sintering [27,35,36]. Due to the low self diffusion coefficient, additives such as B₄C [15,18,36], carbon [15,31], TaB₂ [16,31] and TaSi₂ [34] have also been utilized to aid the sintering.

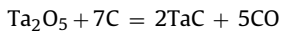
In the present study, we have synthesized TaC composites reinforced with carbon nanotubes (CNTs) using spark plasma sintering. CNTs have proved as effective reinforcement in increasing the fracture toughness of ceramic materials through mechanisms such as crack bridging and crack deflection [37–40]. Improvement in the CNT dispersion leads to significant improvement in fracture and wear properties of the composites and coatings [38,41,42]. Carbon fiber reinforced TaC composites have been prepared by infiltration of carbon fiber weave Ta and C containing solutions followed by vacuum sublimation treatments [43]. Recently, Khaleghi et al. have synthesized a TaC–0.77 wt.% CNT composite using spark plasma sintering. The relative density of the composite synthe-

* Corresponding author. Tel.: +1 305 348 1701; fax: +1 305 348 1932.
E-mail address: agarwala@fu.edu (A. Agarwal).

sized at 2300 °C and 30 MPa pressure increased from 92% to 96%, while the rupture strength increased from 336 to 550 MPa due to addition of CNTs. Carbon has also been reported to play an important role as a sintering aid [15,31] and grain growth inhibitor [15].

In the current study, the overall carbon concentration is 10.2 wt.% in Ta–C phase diagram near an eutectic of TaC and C. The addition of 4 wt.% carbon nanotubes is expected to have the following benefits:

- Improved fracture toughness of TaC.
- CNTs are expected to suppress grain growth and simultaneously aid densification [15,31,44].
- It is envisaged that CNTs would reduce the decomposition of TaC to Ta₂C by providing extra carbon. Although TaC is extremely stable, but under vacuum plasma spraying conditions it decomposes to Ta₂C [22].
- The oxidation resistance of TaC may be improved by suppressing formation of Ta₂O₅. Ta₂O₅ can be converted to TaC by the following reaction:



($\Delta G = 1142.3 - 0.823 \times T$ [45], –ve for $T > 1388$ K).

Multi-walled CNTs of two different lengths have been employed to evaluate the “length effect” on the densification, grain-growth and reinforcement efficiency. The effect of powder preparation technique leading to differences in CNT dispersion is elucidated. Spark plasma sintering was carried at 1850 °C for three pressures of 100, 255 and 363 MPa. The effect of the pressure on the grain size and densification behavior is also studied. This is a first study on TaC–CNT composites at such extreme pressures and temperatures in SPS environment, which also examines the structural stability of CNTs under the severe conditions.

2. Experimental

2.1. Powder preparation

Fine tantalum carbide powder (average particle size = $0.36 \pm 0.13 \mu\text{m}$) was obtained from Inframat Advanced Materials LLC, CT, USA. The composition of the powder by weight was a purity of 99.7% with total carbon $\geq 6.2\%$, free carbon $\leq 0.15\%$, Nb $< 0.3\%$, and O between 0.15 and 0.3%. Two kinds of multi-walled carbon nanotubes (CNTs) were employed in the study, long and short CNTs. The long –COOH group functionalized CNTs were obtained from Nanostructured and Amorphous Materials Inc., TX, USA, and were more than 95% pure and had a diameter of 30–50 nm and length between 10 and 20 μm . The shorter CNTs were obtained from Inframat Advanced Materials (Willington, CT, USA), and had a purity of more than 95%, diameter of 40–70 nm and length 1–3 μm . SEM images of TaC powder, long and short CNTs are shown in Fig. 1.

It is critical that CNTs are uniformly distributed in the matrix. Two different approaches were carried out for dispersing 4 wt.% CNTs in TaC powder. In the first approach using wet chemistry technique, 1 g of long CNTs were added to 100 ml of acetone in a beaker and ultrasonicated for 90 min. Subsequently, 24 g of TaC powder was added and the mixture was ultrasonicated again for 90 min. The mixture was allowed to dry for 12 h and then crushed to obtain the TaC–4 wt.% long CNT powder, which has been referred to as TaC–LC powder. The second approach included spray drying [46–48]. In this method, TaC powder and 4 wt.% short CNTs were added to prepare a water based slurry using a small amount of water soluble polymeric binder. The slurry is then atomized in a column where hot air is passed from the bottom. The droplet of the slurry dry up as they descent through the column and result in agglomerates. The binder helps in providing strength to the agglomerates. By this method, good dispersion of CNTs within micro- and nano-

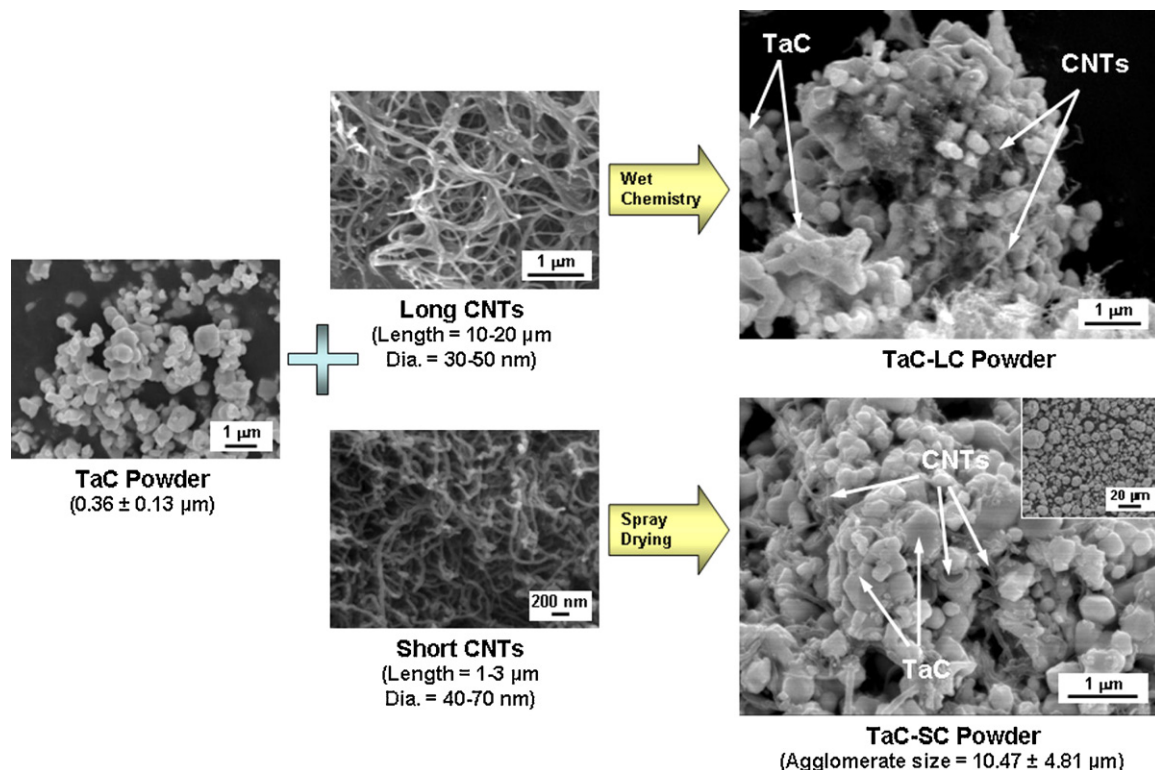


Fig. 1. SEM images showing starting TaC powder, the two kinds of CNTs used in the study and the composite powder mixtures prepared using wet chemistry and spray drying routes.

sized particles can be obtained [37,49]. The spray dried TaC–4 wt.% short CNT powders have been named as TaC–SC powder.

2.2. Spark plasma sintering

Spark plasma sintering (SPS) was utilized to consolidate TaC and the TaC–CNT powders. SPS was carried out in Argon atmosphere at 1850 °C. The heating rate of 200 °C min⁻¹ was adopted to reach the maximum temperature with a hold time of 10 min. SPS was carried out at three different pressures of 100 MPa, 255 MPa and 363 MPa. The 100 MPa samples were approximately 4–5 mm thick and 20 mm in diameter and were prepared using graphite dies and punches. The samples sintered at 255 and 363 MPa had a thickness of 2–3 mm and were prepared in a 10 mm diameter silicon carbide die with silicon carbide punches. SPS was carried out at Thermal Technology LLC, CA, USA. Hereafter, the TaC samples prepared at 100, 255 and 363 MPa pressure have been named as TaC-100, TaC-255 and TaC-363 respectively. Similarly, samples prepared from the TaC–4 wt.% long CNT powders at a pressure of 100, 255 and 363 MPa have been named as TaC–LC-100, TaC–LC-255 and TaC–LC-363 respectively. The samples prepared from spray dried TaC–4 wt.% short CNT powders at a pressure of 100, 255 and 363 MPa have been named as TaC–SC-100, TaC–SC-255 and TaC–SC-363 respectively.

2.3. Microstructural characterization

Sintered TaC samples were ground using SiC paper to remove the graphite foil attached on all surfaces. Subsequently, the bulk density was measured using water immersion technique. The relative density of the TaC samples was calculated as a % of true density, which was measured for the powders using Helium gas pycnometer (Accupyc 1340, Micromeritics Instrument Corporation, Norcross, GA, USA) to be 14.67 g cm⁻³. The relative density of the TaC–CNT samples was calculated as % of the theoretical density, which was calculated from the rule of mixtures, to be 11.84 g cm⁻³ taking the true density of CNTs to be 2.1 g cm⁻³ [49]. Metallographic samples were prepared by grinding until 600 grit SiC paper and then polished using diamond suspension until 0.1 μm finish. Fracture surface of the SPS samples were prepared by breaking the samples with a hammer and observing normal to the fracture surface. A JEOL JSM 630F scanning electron microscope (SEM) with a field emission gun was used to study the morphology of the powders and fracture surfaces. X-ray diffraction was carried out using a Bruker D500 X-ray Diffractometer using Cu–Kα X-rays at a scan rate of 1°/min. A Philips/FEI Tecnai F30 transmission electron microscope (TEM) using a field emission gun and operating at an accelerating voltage of 300 kV was used to study the microstructure. To study the effect of the processing conditions on the CNT structure, micro-Raman spectroscopy was carried out in the backscattering mode using an Argon ion laser of wavelength 514.5 nm and 18 mW.

2.4. Mechanical property characterization

Nanohardness and elastic modulus of the sintered compacts were measured by nanoindentation on the polished cross section. A Triboindenter (Hysitron Inc., Minneapolis, MN, USA) was used to carry out the tests. Indentations were carried out at a load of 4.5 mN. The load function comprises loading to 4.5 mN in 10 s followed by holding at maximum load for 2 s and then unloading to zero load in 10 s. The reduced elastic modulus obtained from nanoindentation (E_r) by the Oliver and Pharr method was corrected for the deformation of the indenter, which is significant due to the high elastic modulus/hardness of the samples, using the following equation.

$$\frac{1}{E_r} = \frac{1 - \nu_s^2}{E_s} + \frac{1 - \nu_i^2}{E_i} \quad (1)$$

Here E_s is the actual elastic modulus of the sample, and ν_s is the Poisson's ratio of TaC which is taken equal to 0.24 [30], E_i and ν_i are the elastic modulus and Poisson's ratio of the indenter which is taken equal to 1141 GPa and 0.07 [50] respectively. Two 5 × 5 indentation test matrices (50 indents) were made at different locations on each of the samples with 9 μm spacing between each indentation.

Fracture toughness was evaluated using a Vickers indenter on the polished cross section using a microhardness tester (Shanghai Taiming Optical Instrument Co. Ltd., model HXD-1000 TMC, Shanghai, China) at a load of 500 g and dwell time of 15 s. The crack lengths (c) were measured from the center of the indents and the fracture toughness K_{IC} was computed using the Anstis equation [51]:

$$K_{IC} = 0.016 \left(\frac{E}{H} \right)^{1/2} \frac{P}{c^{3/2}} \quad (2)$$

where E is the elastic modulus, H is the hardness and P is the load applied (500 g).

3. Results and discussion

3.1. Powder characteristics

Fig. 1 shows the high magnification SEM images of the TaC–LC and TaC–SC powders after the mixing processes. The long CNTs were found to be distributed between the sub-micron TaC particles by the wet chemistry method. Some CNT clusters were also observed. The long length of entangled CNTs makes it difficult to separate entirely by ultrasonication. On the other hand, spray drying leads to formation of spherical agglomerates of TaC–SC powder (inset in Fig. 1). The average size of the spherical TaC–SC composite agglomerates is 10.5 ± 4.8 μm. The high magnification image shows that the CNTs are uniformly distributed on the surface. The distribution of the CNTs is better in case of TaC–SC powder which could be partially attributed to the smaller length of the CNTs.

3.2. Density and microstructure of the TaC–CNT composites

The density of the composites as measured by water immersion technique is tabulated in Table 1. Fig. 2 shows the variation of the density of the composites as a function of SPS pressure for TaC, TaC–LC and TaC–SC powders. Addition of CNTs increases the density of TaC sample prepared at 100 MPa from 89% to 95% for both short and longer CNTs. This could be due to the fact that CNTs are able to occupy the fine porous regions between the TaC grains (as seen in Fig. 4 later) due to their small size. Also, CNTs are expected

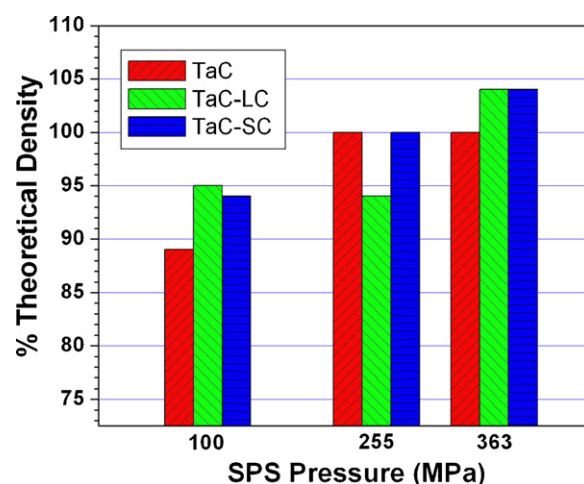


Fig. 2. Variation of the density of the composites as a function of SPS pressure.

Table 1
Properties of TaC and TaC–4 wt.% CNT compacts prepared by SPS.

Powder	SPS compact	Density (g cm ⁻³)		Grain size (μm)	Nano-hardness (GPa)	Elastic modulus (GPa)	Relative fracture toughness
		Actual	Relative (%)				
TaC	TaC-100	13.0	89	0.56 ± 0.12	17.8 ± 3.2	335 ± 28	^a
	TaC-255	14.6	100	4.93 ± 1.99	26.3 ± 2.7	469 ± 46	1 ^b
	TaC-363	14.6	100	5.6 ± 2.4	25.7 ± 5.7	457 ± 39	0.99 ± 0.09
TaC–4 wt.% long CNTs	TaC–LC-100	11.3	95	0.61 ± 0.27	22.9 ± 2.1	395 ± 17	^a
	TaC–LC-255	11.1	94	1.06 ± 0.34	14.2 ± 1.8	288 ± 29	1.58 ± 0.04
	TaC–LC-363	12.3	104	1.22 ± 0.43	12.7 ± 0.7	369 ± 18	1.60 ± 0.12
Spray dried TaC–4 wt.% short CNTs	TaC–SC-100	11.1	94	1.85 ± 0.72	17.5 ± 2.4	331 ± 47	^a
	TaC–SC-255	11.8	100	1.64 ± 0.38	14.7 ± 2.5	313 ± 37	1.44 ± 0.21
	TaC–SC-363	12.3	104	1.65 ± 0.44	10.6 ± 1.2	258 ± 14	1.08 ± 0.18

^a Indentation fracture toughness was not measured due to porous nature of the compact.

^b Fracture toughness of TaC–BC-255 was taken as the reference for normalizing indentation toughness values.

to improve the heat transfer due to increased thermal conductivity [52] which will enhance diffusion and aid densification. Larger increase in density has been observed by addition of CNTs than carbon black in case of spark plasma sintered Al₂O₃ [53]. For the 255 MPa pressure samples, the TaC–LC shows the same density as 100 MPa sample while TaC and TaC–SC samples attain full density. The lower (95%) density of TaC–LC-255 sample is attributed to the possible hindrance to the grain boundary motion due to

longer CNTs which opposes not only grain growth but also densification. The short CNTs however, may not pose as much resistance to boundary motion and are also able to enter the micro-pores between TaC grains. All samples attained full density at 363 MPa pressure. It is suggested that longer CNTs in TaC–LC sample undergo significant deformation at higher pressure of 363 MPa resulting in full density as opposed to 255 MPa. The larger than 100% density measured for 363 samples is attributed to the fact that hollow cylin-

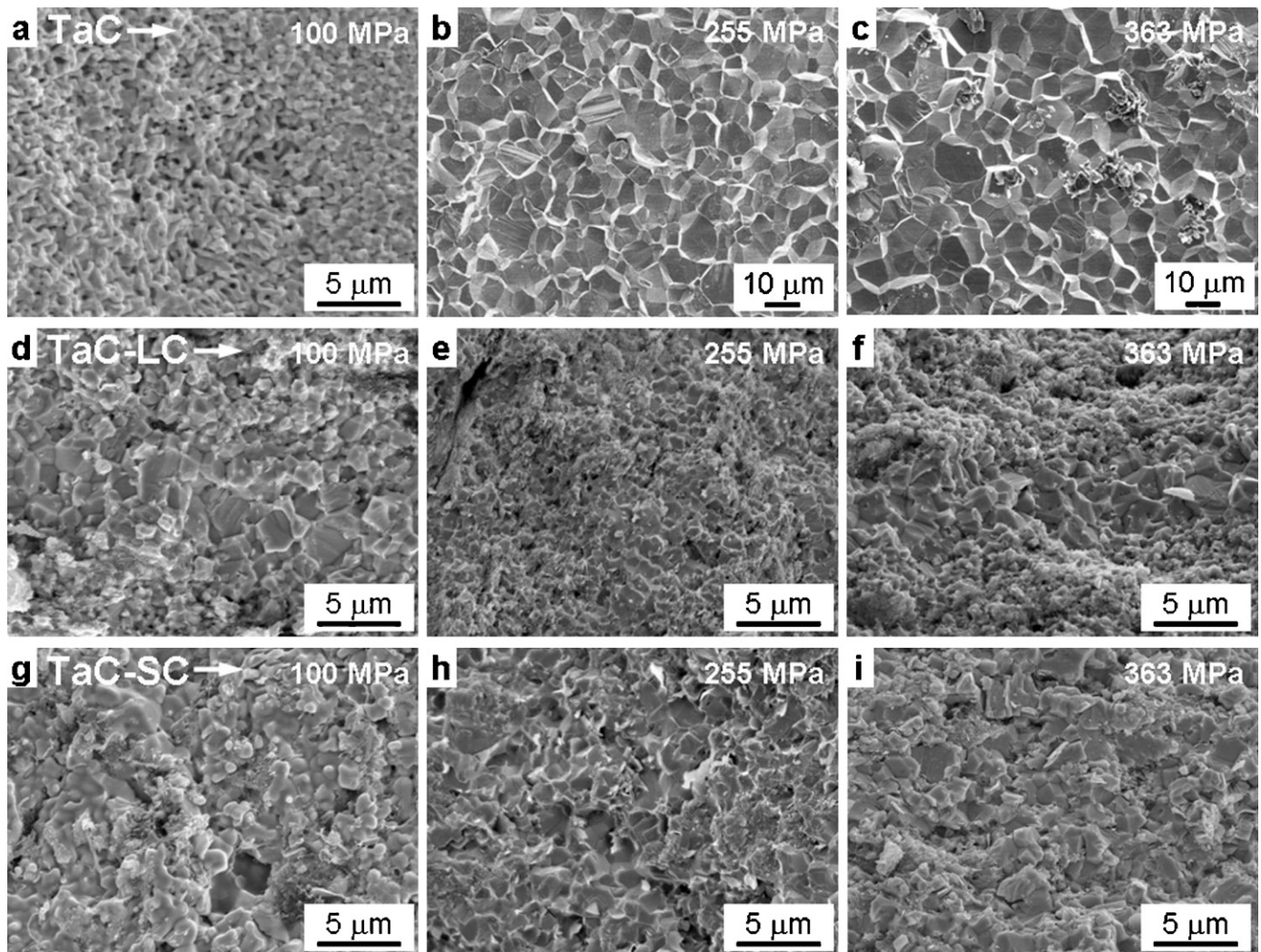


Fig. 3. SEM images showing the fracture surfaces of the TaC (a–c), TaC–LC (d–f) and TaC–SC (g–i) elucidating different grain morphologies. Note the lower magnification required in b and c to see the grain structure.

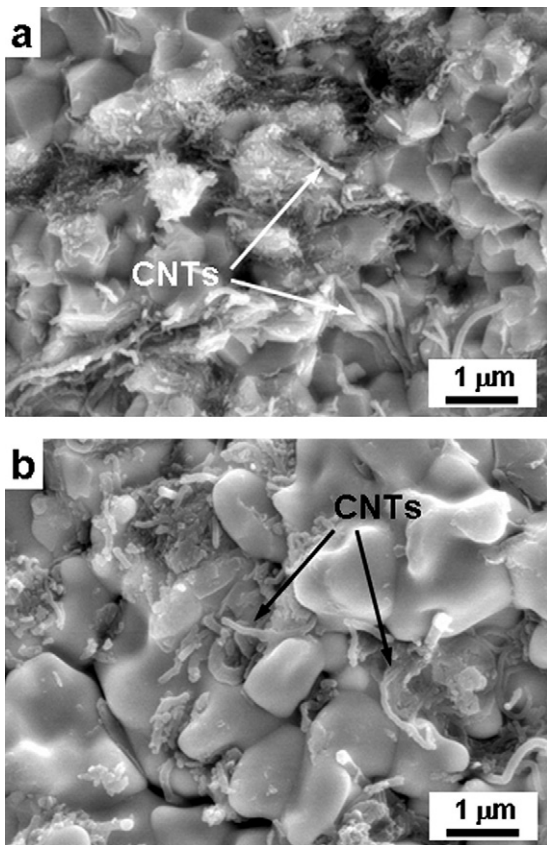


Fig. 4. High magnification SEM images of the fracture surface of (a) TaC-LC-100 and (b) TaC-SC-100 samples showing different grain morphologies and presence of intact CNTs.

drical CNTs are transformed to flaky graphite (which is discussed later in Section 3.4), which has a higher true density of 2.3 g cm^{-3} .

Fig. 3 shows the fracture surfaces of TaC, TaC-LC and TaC-SC samples prepared at different pressures. It is observed that except the TaC-100 sample (Fig. 3a), all other samples appear dense as they have 95% or more relative density. TaC-255 and TaC-363 samples show significant grain growth while TaC-LC and TaC-SC samples show a fine grained structure even at highest pressure of 363 MPa. The fracture surface of TaC samples synthesized at 255 MPa and 363 MPa shows a faceted morphology corresponding to inter-granular failure. TaC-100 and TaC-LC-100 samples also show a faceted morphology except that there are lots of pores in inter-particle region in TaC-100 sample. The TaC-SC-100 sample (Figs. 3g and 4b) shows smoother fracture surface with rounded grains suggesting some degree of melting.

Fig. 4 shows high magnification SEM images of the fracture surfaces of TaC-LC-100 and TaC-SC-100 samples. The presence of intact CNTs can be clearly observed in both composites. The rounder and smooth morphology of the grains (Fig. 4b) in TaC-SC-100 samples suggest that TaC has undergone partial melting during the process. This indicates a local temperature rise which could be due to the joule heating of the CNTs. Individual multiwall CNTs have a high thermal conductivity of up to 3000 W m K^{-1} [54] which could help in increasing the heat transfer characteristics of the powder compact during SPS. The better dispersion and the shorter length of the CNTs would result in increased thermal conductivity [55] in case of the TaC-SC powder leading to partial melting. This elucidates the importance of CNT distribution in influencing the final microstructure. Fig. 5 shows a high magnification SEM image of the fracture surface of the TaC-SC-100 sample showing a re-solidified

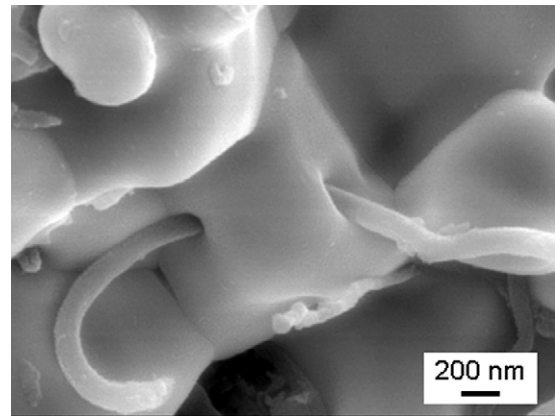


Fig. 5. High magnification SEM image of TaC-SC-100 sample showing molten TaC particle encapsulating a CNT.

TaC particle encapsulating a CNT. Such encapsulation of CNT inside a TaC particle is not possible without local melting of TaC. This indicates that the CNTs are the source of the heat (by joule heating) and also indicates that CNTs can survive such high temperatures. It is expected that encapsulated CNTs will act as links connecting grains and lead to strengthening and toughening.

3.3. CNTs as grain growth inhibitors

The grain size was measured from the SEM images at different magnifications using the software Image J. Only those grains were considered which were half or more visible on the fracture surface. More than 50 grains values were considered to obtain the average value which is tabulated in Table 1. Fig. 6 shows the variation of average grain size of TaC in the sintered compacts as a function of SPS pressure. The error bars indicate the standard deviation. It is clearly observed that CNTs act as hindrances to grain boundary motion and inhibit grain growth. In the case of TaC-LC sample (Fig. 3d–f), the regions in the center of the microstructure are observed to have larger grains than the periphery. At higher magnification as shown in Fig. 7, the grain boundaries of the larger grains are clean or have lesser CNTs at the interfaces and hence had higher grain growth rate. Thus, it can be concluded that the CNTs present in the inter-granular regions act as pinning agents which decrease grain mobility. A similar behavior has also been observed in case of plasma sprayed Al_2O_3 -CNT composites [44].

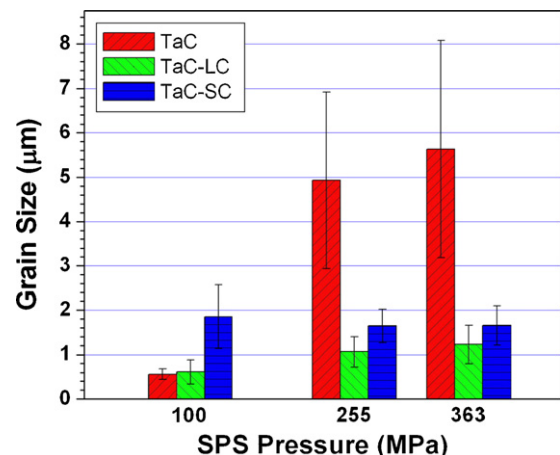


Fig. 6. Variation of TaC grain size of the samples with SPS pressure.

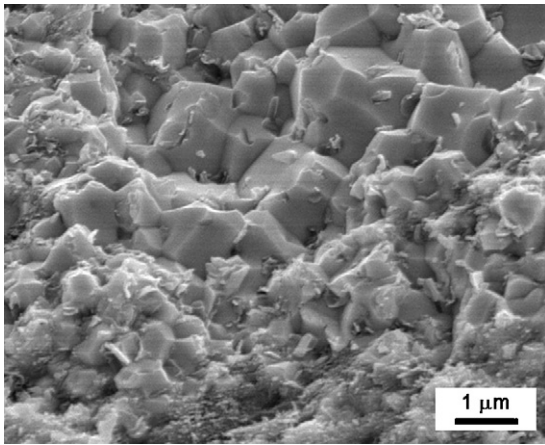


Fig. 7. SEM image of fracture surface of TaC-LC-363 sample showing regions of different grain sizes. Note that the regions with higher CNTs at the boundaries are fine grained while the inter-granular regions of the larger grains are CNT free.

Al_2O_3 composites prepared by SPS at 1100–1900 °C and 100 MPa pressure have also shown that CNTs are more effective than carbon black in reducing the grain growth [53]. The average grain size of TaC-SC is larger than TaC-LC for all pressures. This indicates that longer CNTs are more effective in pinning the grain boundaries and offer more resistance to their movement without much influence from pressure. This seems obvious since longer CNTs can cover more inter-granular surface area and hence are more effective.

3.4. Stability of CNTs in SPS

The structural stability of the CNTs is essential for the toughening to occur. In SPS, the CNTs are subjected to the most severe conditions of heat, pressure and electric current. As observed in Figs. 4 and 5, most of the CNTs were found to be retained with their cylindrical structure intact after being subjected to 100 MPa pressure at 1850 °C. Imam et al. have shown presence of CNTs at the grain boundaries of Al_2O_3 -2 wt.% CNT composite prepared by SPS at 1800 °C and 100 MPa, although they look damaged in the fracture surface [53]. Intact CNTs have also been observed in HA-CNT composites prepared by SPS at 1100 °C and 50 MPa [56] and 60 MPa pressure [57]. However, TEM images showed some CNTs to be damaged at 60 MPa pressure. In bulk CNT compacts prepared by SPS at 2000 °C and 80 MPa pressure, CNTs were also seen intact with partial graphitization [58]. CNTs were also retained in bulk CNT composites synthesized by SPS at 1600 °C and 60 MPa pressure [59]. Zhang et al. have reported damage to CNTs and formation of submicron sized diamond during SPS at 1500 °C and 80 MPa pressure [60]. In a recent study on SPS of Al_2O_3 -CNT samples, Huang et al. have shown that using insulating BN layer on the graphite punch tips helped prevent damage to CNTs indicating that the damage occurred when current passed through the sample [61].

Fig. 8a shows the Raman spectra of the long CNTs and sintered TaC-LC samples. Similarly, Fig. 8b shows the Raman spectra of the short CNTs and sintered TaC-SC samples. Raman peaks for CNTs are generally observed at 1348 cm^{-1} (D-peak), 1574 cm^{-1} (G-peak) and at 2691 cm^{-1} (G'-peak or 2D peak) [62]. The G-peak corresponds to the C-C stretching mode while the D peak arises due to the presence of disorder and sp^3 defects. Table 2 tabulates the peak positions and the ratio of the intensity of the D to G peak (I_D/I_G). It is clearly observed that the D and G peaks shift to higher wave numbers in the SPS samples as compared to free CNTs. This indicates the presence of a compressive stress. The CNTs get com-

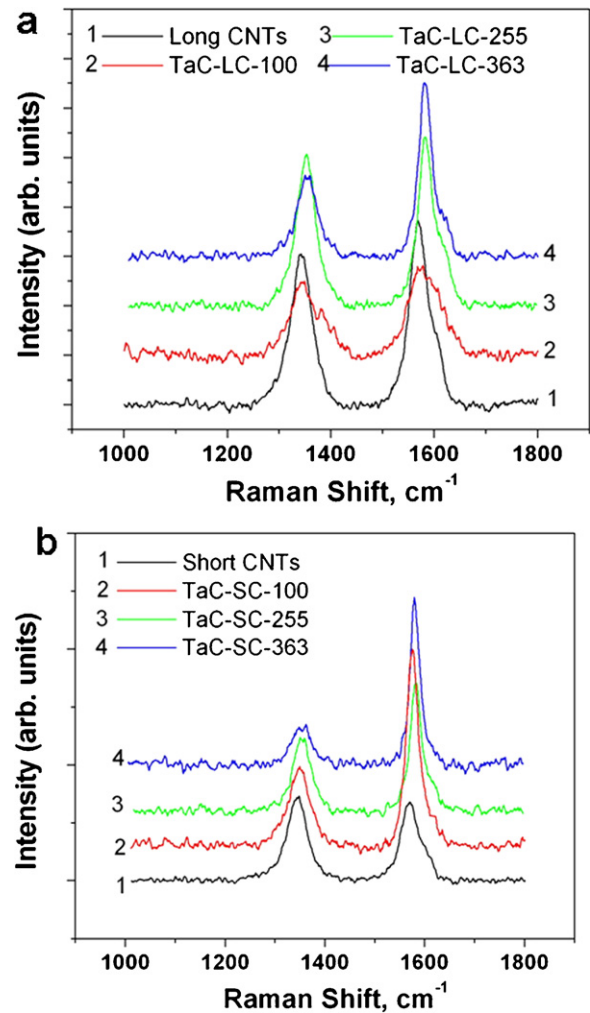


Fig. 8. Raman spectra showing the D and G peaks from carbon nanotubes in (a) TaC-LC samples and (b) TaC-SC samples.

pressed between the TaC grains under the pressure applied during SPS. As sintering progresses, the grains coalesce and the stress on the CNTs remains after processing. Another important observation can be obtained from the I_D/I_G ratio of the D and G peaks. The I_D/I_G ratio for long CNTs is 0.81 which reduces to 0.46 in TaC-LC-363 sample. The I_D/I_G ratio for short CNTs is 1.07 which reduces to 0.23 in TaC-SC-363 sample. Raman spectra of highly ordered pyrolytic graphite (HOPG) consists of just the G peak ($I_D/I_G = 0$) [62]. So the decreasing I_D/I_G trend indicates the conversion of CNTs to graphite like structures. This observation is different from Huang et al. who observed increase in I_D/I_G due to passage of current through CNTs leading to CNT damage [61]. It seems that the pressure greater than 255 MPa causes graphitizing the CNTs. Table 2 also indicates that the shorter CNTs show higher decrease in I_D/I_G ratio indicating shorter CNTs are easily graphitized.

Fig. 9 shows the high magnification SEM images of the fracture surface of TaC-LC-363 and TaC-SC-363 samples. It is observed that while some cylindrical structures are still visible in TaC-LC sample, most of the CNTs in TaC-SC have converted to a layered and flaky morphology in the inter-granular region. This indicates that CNTs are getting graphitized under the combined effect of pressure and temperature during SPS. To further study the damage occurring to CNTs, TEM was carried out on TaC-LC-363 and TaC-SC-363 samples. Fig. 10 shows the TEM images showing presence of carbonaceous material between TaC grains. From Fig. 10b

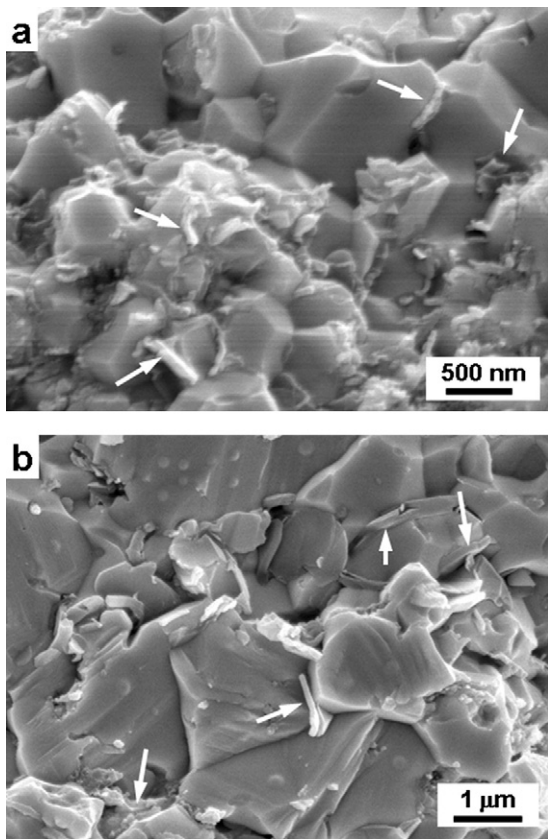


Fig. 9. SEM images of the fracture surface of (a) TaC-LC-363 and (b) TaC-SC-363 sample showing damaged CNTs (white arrows).

and d it is seen that several CNTs are getting damaged and converted to flaky graphitic morphology as was observed in the SEM images (Fig. 9). SEM images of TaC-LC-255 and TaC-SC-255 (not shown here) also indicated similar graphitic morphology of carbon between TaC grains. This indicates that most CNTs were able to survive 100 MPa pressure and 1850 °C, but were getting damaged at higher pressures.

Based on the observations of the Raman spectra, it can be said that the CNTs undergo compressive stresses which could lead to collapse of the cylindrical structure. Buckling of CNTs under hydrostatic compression has been studied earlier using molecular mechanics and atomistic simulations and the collapse of the CNTs leading to formation of ribbons has been reported [63–65]. Continuum mechanics predicts the buckling pressure for collapse of tubes as [65]

$$P_B = \frac{2E}{(1-\nu^2)} \left(\frac{t}{D}\right)^3 \quad (3)$$

where P_B is the buckling pressure, E is the elastic modulus, ν is the Poisson's ratio ($=0.27$), t is the thickness of the tube, and D is the diameter. Using the average values for the dimensions of long CNTs ($t = 16$ nm, $D = 40$ nm) and the values for short CNTs ($t = 19$ nm, $D = 45$ nm) from our previous study [66], the value of P_B turns out to be $0.14E$ for long CNTs and $0.16E$ for short CNTs. The radial elastic modulus of the multiwall CNTs has been measured to be 21 ± 7 GPa at room temperatures [67]. Using these relations it turns out that the pressure required for buckling and collapse of long and short CNTs is ~ 3 GPa at room temperature. However, at the SPS temperature of 1850 °C, collapse is expected to occur at much lower pressures. Collapse of the CNTs into ribbon like flaky structure at high temperatures may lead to conversion of the CNT to graphite.

Table 2

Raman spectra data for peaks from carbon nanotubes from the SPS samples.

Sample	D-peak	G-peak	I_D/I_G
Long CNTs	1343	1569	0.81
TaC-LC-100	1345	1578	0.82
TaC-LC-255	1353	1583	0.89
TaC-LC-363	1355	1582	0.46
Short CNTs	1348	1571	1.07
TaC-SC-100	1349	1578	0.25
TaC-SC-255	1355	1583	0.57
TaC-SC-363	1356	1580	0.23

Collapse and welding of CNTs have been observed at 1500 °C and 7 MPa during SPS of aligned CNTs, which indicate that the pressure required for collapse may be quite low at high temperatures [68]. A few of CNTs were also damaged in 100 MPa sintered samples as seen in Fig. 4. The presence of 5–6% porosity leads to entrapment of CNTs in the inter-granular regions. Due to the high hardness of TaC, carbon nanotubes may not feel the applied pressure at 100 MPa, except at the inter-granular contact areas, and hence could be retained. However, the samples prepared at 255 MPa and 363 MPa pressure are fully dense and the pressure is transmitted to most of the CNTs leading to their graphitization at the inter-granular regions.

3.5. Mechanical properties of TaC-CNT composites

Nanohardness and elastic modulus of TaC and TaC-CNT composites measured by nanoindentation are listed in Table 1 and plotted in Figs. 11 and 12 respectively. From Fig. 11 it is observed that the hardness of TaC increases with SPS pressure which can be attributed to the densification. The average values of the nanohardness of TaC is larger than microhardness values (~ 15 GPa) reported in the literature [13,18,33] which is due to the localized nature of the nanoindentation testing. The increased hardness of TaC-LC-100 as compared to TaC-100 is attributed to: (i) increase in the density from 89% to 95% and (ii) indentation resistance provided by long length of the CNTs that help in holding the TaC grains together. However, the shorter CNTs in TaC-SC-100 sample are not able to improve the hardness despite the increase in density, which is not clearly understood. The lower hardness of the TaC-CNT samples prepared at 255 and 363 MPa pressure as compared to TaC samples is attributed to CNTs getting damaged and converting to flaky graphitic structures. It is well known that graphite has a very low hardness as compared to TaC.

Fig. 12 shows that elastic modulus of TaC increases with the SPS pressure which is attributed to the densification. The lower elastic modulus of the TaC-100 sample as compared to TaC-255 and TaC-363 sample is due to the porosity. TaC-LC-100 having a higher density shows an increased elastic modulus as compared to TaC-100 sample. Additionally CNTs have high elastic modulus of 600–1000 GPa [69] which help in increasing the modulus. The lower length of the CNTs in TaC-SC-100 leads to no increase in the elastic modulus despite the increase in density because small CNTs do not effectively share the load applied during indentation. The effect of increased length to diameter ratio (aspect ratio) on increasing the strengthening effect is well known in fiber composites as is elucidated by in micromechanical models such as the Halpin-Tsai model [70,71]. The decrease in the elastic modulus of TaC-CNT samples with increasing SPS pressure is due to the progressive damage to CNTs at higher SPS pressures. Thus, the effective amount of CNTs reinforcing the TaC reduces, while the flaky graphitic structures formed are not expected to contribute towards the increase in stiffness.

Fig. 13 shows the relative fracture toughness of the composites as a function of SPS pressure. The fracture toughness of the 100 MPa

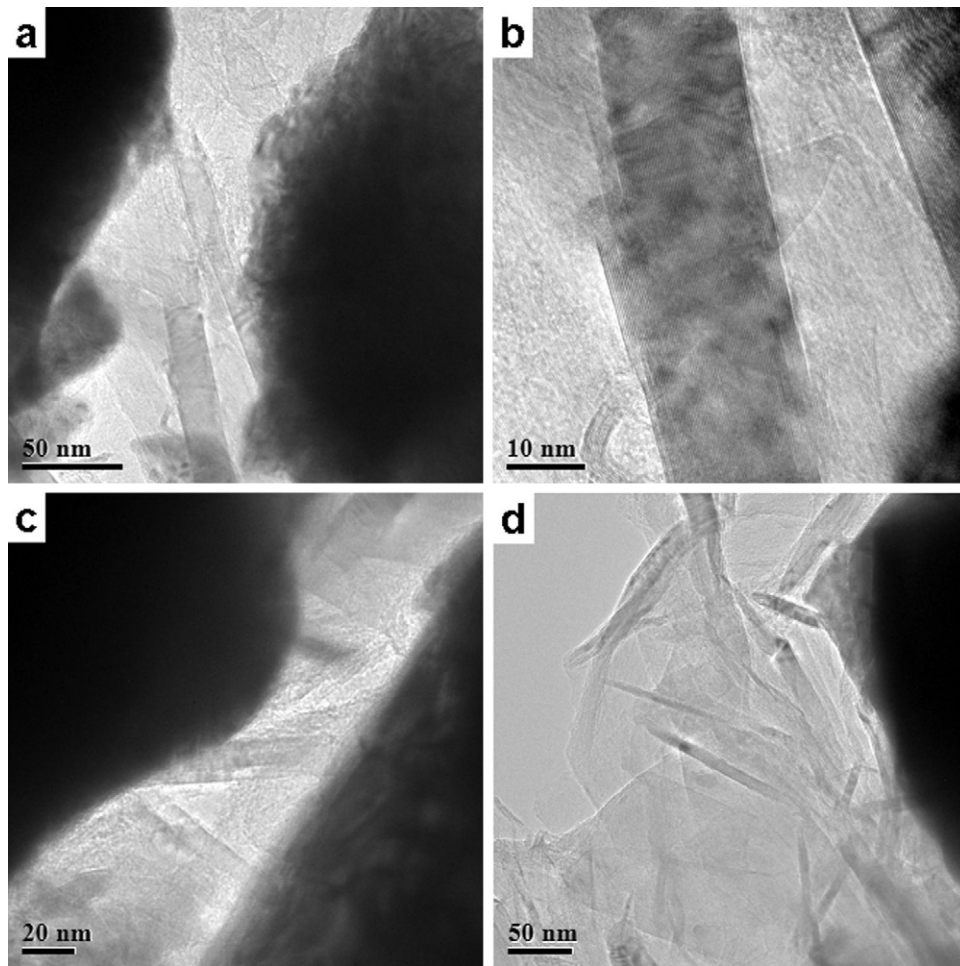


Fig. 10. TEM images of TaC-LC-363 (a and b) and TaC-SC-363 (c and d) samples showing presence of carbonaceous structures between TaC grains and damaged CNT structures.

samples was not considered because of the low density of the reference TaC-100 sample. It is observed that long CNTs are more efficient in increasing the fracture toughness of the samples as compared to shorter ones. TaC-LC-363 sample showed a 60% increase in the fracture toughness compared to TaC-255 sample. However, TaC-SC-363 sample showed very small improvement in the fracture toughness. This is attributed to the more extensive damage

to the shorter CNTs which resulted in decreased toughening effect as observed in Figs. 10 and 11. The effect of long and short CNTs on different aspects (processing, microstructure and mechanical properties) of the TaC-CNT composites is summarized in Table 3. It is observed that the long CNTs are better in enhancing mechanical properties but pose the challenge of uniform dispersion in the matrix.

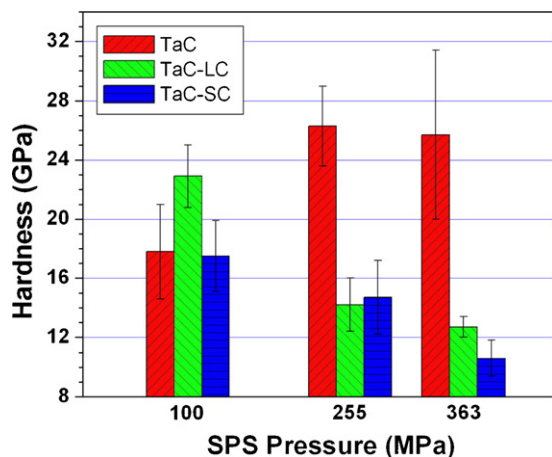


Fig. 11. Variation of hardness of the composites with SPS pressure.

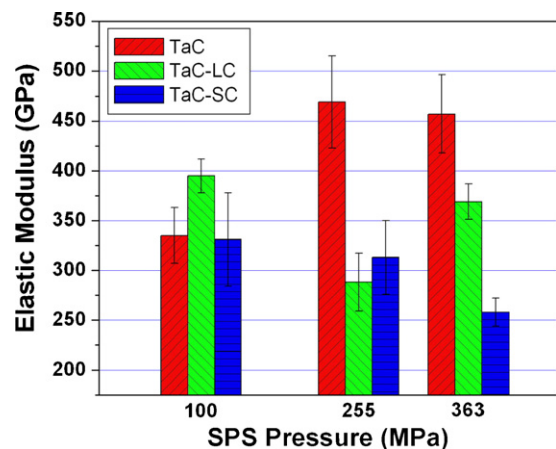


Fig. 12. Variation of elastic modulus of the composites with SPS pressure.

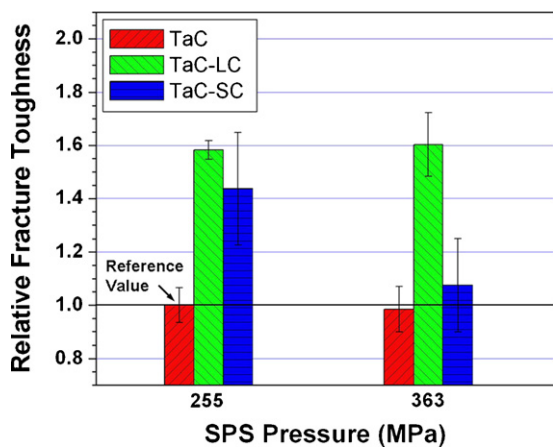


Fig. 13. Relative fracture toughness of sintered TaC, TaC-LC and TaC-SC samples with SPS pressure normalized to the value of TaC-255 sample.

Table 3
A comparison of effect of adding long and short CNTs on TaC-CNT composites.

Property	Long CNT	Short CNT
Dispersion	Difficult to disperse	Relatively easy
Thermal conductivity of mixtures	Smaller enhancement due to decreased length efficiency	Relatively higher enhancement is observed
Extent of graphitization	Relatively lower	Relatively higher
Sintering aid	Good	Good
Grain growth inhibition effect	Good	Relatively poor
Hardness improvement	High	Relatively lower
Elastic modulus improvement	Higher	Relatively lower
Fracture toughness improvement	Higher	Relatively lower

4. Conclusions

TaC composites with 4 wt.% long and short CNTs as reinforcement were synthesized by SPS at various pressures. Spray drying was observed to lead to better dispersion of shorter CNTs compared to wet chemistry technique that was utilized for dispersing longer CNTs. Addition of carbon nanotubes increased the density of TaC from 89% to 95% for the 100 MPa pressure samples. TaC-SC-100 sample showed partial melting of TaC grains which could be due to better thermal conductivity and uniform dispersion of CNTs due to spray drying. CNT act as grain growth inhibitors. The long CNTs were more efficient in pinning the boundaries compared to shorter ones. Damage to CNTs was observed at 255 MPa and higher pressures during SPS. At higher pressures, CNTs converted to flaky graphitic structures. Longer CNTs had better reinforcing effect than shorter CNTs in terms of increasing the elastic modulus, hardness and fracture toughness. Increase in fracture toughness of up to 60% was observed by addition of long CNT for the TaC-LC-363 sample. An optimum CNT length and intermediate SPS pressure could further improve the mechanical properties of TaC-CNT composites.

Acknowledgements

The authors acknowledge financial support from US Air Force Office of Scientific Research (Grant No. FA9550-09-1-0297) and thank Program Officer Dr. Joan Fuller. Dr. Daniela Fredrick's assistance with SPS processing at Thermal Technology, Santa Rosa, CA is greatly acknowledged. Authors are also thankful to AMERI at FIU for providing the research facilities and especially to Mr. Neal Ricks

and Dr. Y. Liu for their assistance. Authors are grateful to CeSMEC at FIU for providing Raman spectra measurement facility.

References

- [1] J. Cotton, *Adv. Mater. Process.* 168 (2010) 26–28.
- [2] F. Monteverde, A. Bellosi, L. Scatteia, *Mater. Sci. Eng. A: Struct. Mater. Prop. Microstruct. Process.* 485 (2008) 415–421.
- [3] E.L. Corral, R.E. Loehman, *J. Am. Ceram. Soc.* 91 (2008) 1495–1502.
- [4] S.R. Levine, E.J. Opila, M.C. Halbig, J.D. Kiser, M. Singh, J.A. Salem, *J. Eur. Ceram. Soc.* 22 (2002) 2757–2767.
- [5] T.H. Squire, J. Marschall, *J. Eur. Ceram. Soc.* 30 (2010) 2239–2251.
- [6] W.G. Fahrenholtz, G.E. Hilmas, I.G. Talmy, J.A. Zaykoski, *J. Am. Ceram. Soc.* 90 (2007) 1347–1364.
- [7] J.X. Liu, Y.M. Kan, G.J. Zhang, *J. Am. Ceram. Soc.* 93 (2010) 370–373.
- [8] Y.J. Yan, Z.R. Huang, S.M. Dong, D.L. Jiang, *J. Am. Ceram. Soc.* 89 (2006) 3589–3592.
- [9] Y.J. Yan, H. Zhang, Z.R. Huang, X.J. Liu, *J. Inorg. Mater.* 24 (2009) 631–635.
- [10] H. Zhang, Y.J. Yan, Z.R. Huang, X.J. Liu, D.L. Jiang, *J. Am. Ceram. Soc.* 92 (2009) 1599–1602.
- [11] A. Balbo, D. Sciti, *Mater. Sci. Eng. A: Struct. Mater. Prop. Microstruct. Process.* 475 (2008) 108–112.
- [12] W.G. Fahrenholtz, G.E. Hilmas, A.L. Chamberlain, J.W. Zimmermann, *J. Mater. Sci.* 39 (2004) 5951–5957.
- [13] K. Hackett, S. Verhoef, R.A. Cutler, D.K. Shetty, *J. Am. Ceram. Soc.* 92 (2009) 2404–2407.
- [14] F. Monteverde, *J. Alloys Compd.* 428 (2007) 197–205.
- [15] X.H. Zhang, G.E. Hilmas, W.G. Fahrenholtz, D.M. Deason, *J. Am. Ceram. Soc.* 90 (2007) 393–401.
- [16] X. Zhang, G.E. Hilmas, W.G. Fahrenholtz, *J. Am. Ceram. Soc.* 91 (2008) 4129–4132.
- [17] X.H. Zhang, L. Xu, S.Y. Du, C.Y. Liu, J.C. Han, W.B. Han, *J. Alloys Compd.* 466 (2008) 241–245.
- [18] X.H. Zhang, G.E. Hilmas, W.G. Fahrenholtz, *Mater. Sci. Eng. A: Struct. Mater. Prop. Microstruct. Process.* 501 (2009) 37–43.
- [19] S.J. Lee, E.S. Kang, S.S. Baek, D.K. Kim, *Surf. Rev. Lett.* 17 (2010) 215–221.
- [20] F. Monteverde, *Compos. Sci. Technol.* 65 (2005) 1869–1879.
- [21] L. Rangaraj, C. Divakar, V. Jayaram, *J. Eur. Ceram. Soc.* 30 (2010) 129–138.
- [22] K. Balani, G. Gonzalez, A. Agarwal, R. Hickman, J.S. O'Dell, S. Seal, *J. Am. Ceram. Soc.* 89 (2006) 1419–1425.
- [23] M. Tului, G. Marino, T. Valente, *Surface, Surf. Coat. Technol.* 201 (2006) 2103–2108.
- [24] Z.A. Munir, U. Anselmi-Tamburini, M. Ohyanagi, *J. Mater. Sci.* 41 (2006) 763–777.
- [25] U. Anselmi-Tamburini, Y. Kodera, M. Gasch, C. Unuvar, Z.A. Munir, M. Ohyanagi, S.M. Johnson, *J. Mater. Sci.* 41 (2006) 3097–3104.
- [26] A. Bellosi, F.D. Monteverde, D. Sciti, *Int. J. Appl. Ceram. Technol.* 3 (2006) 32–40.
- [27] E. Khaleghi, Y.S. Lin, M.A. Meyers, E.A. Olevisky, *Scr. Mater.* 63 (2010) 577–580.
- [28] R. Licheri, R. Orru, C. Musa, A.M. Locci, G. Cao, *J. Mater. Sci.* 43 (2008) 6406–6413.
- [29] F. Monteverde, C. Melandri, S. Guicciardi, *Mater. Chem. Phys.* 100 (2006) 513–519.
- [30] L. Lopez de la Torre, B. Winkler, J. Schreuer, K. Knorr, M. Avalos-Borja, *Solid State Commun.* 134 (2005) 245–250.
- [31] I.G. Talmy, J.A. Zaykoski, M.M. Opeka, *J. Eur. Ceram. Soc.* 30 (2010) 2253–2263.
- [32] M. Desmaison-Brut, N. Alexandre, J. Desmaison, *J. Eur. Ceram. Soc.* 17 (1997) 1325–1334.
- [33] B.R. Kim, K.D. Woo, J.M. Doh, J.K. Yoon, I.J. Shon, *Ceram. Int.* 35 (2009) 3395–3400.
- [34] D. Sciti, L. Silvestroni, S. Guicciardi, D.D. Fabbri, A. Bellosi, *J. Mater. Res.* 24 (2009) 2056–2065.
- [35] L. Liu, F. Ye, Y. Zhou, Z. Zhang, *J. Am. Ceram. Soc.* 93 (2010) 2945–2947.
- [36] S.R. Bakshi, V. Musaramthota, D. Lahiri, V. Singh, S. Seal, A. Agarwal, *Mater. Sci. Eng. A* (2010), doi:10.1016/j.msea.2010.10.009.
- [37] K. Balani, S.R. Bakshi, Y. Chen, T. Laha, A. Agarwal, *J. Nanosci. Nanotechnol.* 7 (2007) 3553–3562.
- [38] A.K. Keshri, J. Huang, V. Singh, W.B. Choi, S. Seal, A. Agarwal, *Carbon* 48 (2010) 431–442.
- [39] Z. Xia, L. Riestler, W.A. Curtin, H. Li, B.W. Sheldon, J. Liang, B. Chang, J.M. Xu, *Acta Mater.* 52 (2004) 931–944.
- [40] Z. Xia, W.A. Curtin, B.W. Sheldon, *J. Eng. Mater. Technol.: Trans. Asme* 126 (2004) 238–244.
- [41] K. Balani, T. Zhang, A. Karakoti, W.Z. Li, S. Seal, A. Agarwal, *Acta Mater.* 56 (2008) 571–579.
- [42] A. Mukhopadhyay, B.T.T. Chu, M.L.H. Green, R.I. Todd, *Acta Mater.* 58 (2010) 2685–2697.
- [43] J.O. Gibson, M.G. Gibson, in: U.S. Patent (Ed.), *Production of Carbon Fiber-Tantalum Carbide Composites*, 1981.
- [44] K. Balani, S.R. Bakshi, D. Lahiri, A. Agarwal, *Int. J. Appl. Ceram. Technol.* (2009), doi:10.1111/j.1744-7402.2009.02385.x.
- [45] C. Bale, P. Chartrand, S.A. Degterov, G. Eriksson, K. Hack, R. Ben Mahfoud, J. Melancon, A.D. Pelton, S. Petersen, *Calphad-Comput. Coupling Phase Diagrams Thermochem.* 26 (2002) 189–228.
- [46] S.J. Lukasiewicz, *J. Am. Ceram. Soc.* 72 (1989) 617–624.
- [47] X.Q. Cao, R. Vassen, S. Schwartz, W. Jungen, F. Tietz, D. Stoever, *J. Eur. Ceram. Soc.* 20 (2000) 2433–2439.

- [48] V. Viswanathan, K.E. Rea, A. Vaidya, S. Seal, *J. Am. Ceram. Soc.* 91 (2008) 379–386.
- [49] S.R. Bakshi, V. Singh, S. Seal, A. Agarwal, *Surf. Coat. Technol.* 203 (2009) 1544–1554.
- [50] K. Park, S. Mishra, G. Lewis, J. Losby, Z.F. Fan, J.B. Park, *Biomaterials* 25 (2004) 2427–2436.
- [51] G.R. Anstis, P. Chantikul, B.R. Lawn, D.B. Marshall, *J. Am. Ceram. Soc.* 64 (1981) 533–538.
- [52] R. Sivakumar, S.Q. Guo, T. Nishimura, Y. Kagawa, *Scr. Mater.* 56 (2007) 265–268.
- [53] F. Inam, H.X. Yan, T. Peijs, M.J. Reece, *Compos. Sci. Technol.* 70 (2010) 947–952.
- [54] P. Kim, L. Shi, A. Majumdar, P.L. McEuen, *Phys. Rev. Lett.* 87 (2001).
- [55] P.C. Song, C.H. Liu, S.S. Fan, *Appl. Phys. Lett.* 88 (2006).
- [56] S. Kalmodia, S. Goenka, T. Laha, D. Lahiri, B. Basu, K. Balani, *Mater. Sci. Eng. C* (2010), doi:10.1016/j.msec.2010.1006.1009.
- [57] D. Lahiri, V. Singh, A.K. Keshri, S. Seal, A. Agarwal, *Carbon* 48 (2010) 3103–3120.
- [58] M. Uo, T. Hasegawa, T. Akasaka, I. Tanaka, F. Munekane, M. Omori, H. Kimura, R. Nakatomi, K. Soga, Y. Kogo, F. Watari, *Bio-Med. Mater. Eng.* 19 (2009) 11–17.
- [59] J.L. Li, G.Z. Bai, J.W. Feng, W. Jiang, *Carbon* 43 (2005) 2649–2653.
- [60] F.M. Zhang, J. Shen, J.F. Sun, Y.Q. Zhu, G. Wang, G. McCartney, *Carbon* 43 (2005) 1254–1258.
- [61] Q. Huang, D. Jiang, I.A. Ovid'ko, A. Mukherjee, *Scr. Mater.* 63 (2010) 1181–1184.
- [62] M.S. Dresselhaus, A. Jorio, M. Hofmann, G. Dresselhaus, R. Saito, *Nano Lett.* 10 (2010) 751–758.
- [63] J. Xiao, B. Liu, Y. Huang, J. Zuo, K.C. Hwang, M.F. Yu, *Nanotechnology* 18 (2007).
- [64] B.I. Yakobson, C.J. Brabec, J. Bernholc, *Phys. Rev. Lett.* 76 (1996) 2511–2514.
- [65] S.L. Zhang, R. Khare, T. Belytschko, K.J. Hsia, S.L. Mielke, G.C. Schatz, *Phys. Rev. B* 73 (2006).
- [66] S.R. Bakshi, V. Singh, D.G. McCartney, S. Seal, A. Agarwala, *Scr. Mater.* 59 (2008) 499–502.
- [67] L. Muthaswami, Y. Zheng, R. Vajtai, G. Shehkawat, P. Ajayan, R.E. Geer, *Nano Lett.* 7 (2007) 3891–3894.
- [68] K. Yang, J. He, Z. Su, J.B. Reppert, M.J. Skove, T.M. Tritt, A.M. Rao, *Carbon* 48 (2010) 756–762.
- [69] B. Peng, M. Locascio, P. Zapol, S.Y. Li, S.L. Mielke, G.C. Schatz, H.D. Espinosa, *Nat. Nanotechnol.* 3 (2008) 626–631.
- [70] J.C. Halpin, J.L. Kardos, *Polym. Eng. Sci.* 16 (1976) 344–352.
- [71] M.K. Yeh, N.H. Tai, J.H. Liu, *Carbon* 44 (2006) 1–9.



Computational estimation of elastic properties of spark plasma sintered TaC by meshfree and finite element methods

Srinivasa R. Bakshi^{a,b}, Akanksha Bhargava^a, Seyedreza Mohammadzadeh^a, Arvind Agarwal^a, Igor Tsukanov^{a,*}

^aMechanical and Materials Engineering, Florida International University, Miami, FL 33174, USA

^bMetallurgical and Materials Engineering, Indian Institute of Technology Madras, Chennai, India

ARTICLE INFO

Article history:

Received 24 January 2011
Received in revised form 30 March 2011
Accepted 8 April 2011
Available online 4 May 2011

Keywords:

Meshfree method
OOF2
Elastic modulus prediction
Tantalum carbide

ABSTRACT

In this study, the overall elastic modulus of spark plasma sintered TaC composite has been estimated using a novel engineering analysis technique, called Scan-and-Solve, that makes it possible to perform completely automated stress analysis directly from the segmented micrographs. The computed results have been compared with object oriented finite element technique (OOF), which also makes use of the microstructure. In contrast with the traditional mesh based engineering analysis methods, Scan-and-Solve uses spatial meshes that may or may not conform to the shape of the geometric model. This makes Scan-and-Solve computational technology essentially *meshfree*, and it makes it possible to eliminate error-prone and time consuming data conversion and spatial meshing. The presented method guarantees exact treatment of the prescribed boundary conditions. In the paper, we compare the stress simulation results in porous TaC ceramic obtained by the Scan-and-Solve and object oriented finite element methods. It is shown that the effective elastic modulus predicted from the microstructure by the two methods is very similar (266 vs. 270 GPa) provided the porosity coefficients are measured close to each other.

© 2011 Elsevier B.V. All rights reserved.

1. Introduction

Prediction of the overall property of multi-phase materials is an age old problem that dates back to Maxwell's theory. A lot of research work has been devoted towards the prediction of the overall mechanical and thermal properties of multi-phase materials [1–5]. Several analytical models have been developed which take into account the shape and volume fraction of the second phase particles to predict the overall property. However, in most practical cases, the second phase is irregular in shape and assuming it to be a regular shape leads to errors in the prediction. Microstructure based finite element modeling has the key advantage of being able to take the variation of the actual shape and size of second phase and numerically compute the overall response of the microstructure based on the applied boundary conditions. In a previous study, we had used object oriented finite element method (OOF) to compute and accurately predict the thermal conductivity of Al–Si–Carbon nanotube composite at various length scales using corresponding microstructural images [6].

However, the creation of the mesh conforming to the boundary of the second phase in the microstructure could be time consuming as well as requires significant expertise. A mesh having a high

homogeneity and low shape energy is desired [7,8]. Recently, meshfree computations have been investigated for similar applications [9]. In the present work, the overall elastic modulus of spark plasma sintered TaC and TaC–1 wt.% B₄C composite has been estimated using OOF method and Scan-and-Solve meshfree approach. In contrast with the traditional mesh based engineering analysis methods, Scan-and-Solve uses spatial meshes that may or may not conform to the shape of the geometric model. This makes Scan-and-Solve computational technology essentially *meshfree*, and it makes it possible to eliminate error-prone and time consuming data conversion and spatial meshing. The presented method guarantees exact treatment of the prescribed boundary conditions. In addition, it also exhibits exponential convergence and enables adaptive solution refinement by increasing the order the basis functions and/or resolution of the spatial grid. The results of the two techniques are compared and discussed in detail. Meshfree computation is suggested as a viable method for analyzing stress distribution in the complex microstructure and predicting overall mechanical properties of the multi-phase materials.

2. Experimental techniques

Tantalum carbide powder was obtained from Inframat Advanced Materials LLC, CT, USA. The specifications on the composition by weight was a purity of 99.7% with total carbon $\geq 6.2\%$, free

* Corresponding author. Tel.: +1 954 829 6311; fax: +1 305 348 1932.

E-mail address: igor.tsukanov@gmail.com (I. Tsukanov).

carbon $\leq 0.15\%$, Nb $< 0.3\%$, and O between 0.15% and 0.3%. The mean TaC particle size measured from SEM image was $0.36 \pm 0.13 \mu\text{m}$. Boron carbide nanopowder was obtained from MTI Corporation, CA, USA. The average particle size was specified as 50 nm and the purity level was 98%. Boron carbide nanopowder was dispersed in TaC by using ultrasonication technique as described in our previous paper [10]. SPS was carried out in Argon atmosphere to consolidate the powder mixtures. TaC powder was consolidated at 2200 °C and 60 MPa pressure with a 5 min hold time. The TaC-B₄C sample was consolidated at 1850 °C at a pressure of 100 MPa and a hold time of 10 min. The heating rate of 150 °C min⁻¹ was adopted to reach the maximum temperature. The samples were approximately 4–5 mm thick and 20 mm in diameter. TaC sample will be referred to as TaC-2200, while the TaC-B₄C sample will be referred to as TaC-BC-1850. SEM images of fracture surface of TaC-2200 sample was obtained using a JEOL JSM 630F scanning electron microscope (SEM) with a field emission gun, while the back scattered image of the polished cross section of TaC-BC-1850 sample was obtained using a FEI-Phenom SEM. Nanoindentation was carried out using a Hysitron Triboindenter (Hysitron Inc., Minneapolis, MN, USA) to measure the elastic modulus of the matrix region of the coatings. Indentations were carried out at a load of 4.5 mN and the reduced elastic modulus obtained from nanoindentation (E_r) by the Oliver and Pharr method. Two 5×5 indentation test matrices (50 indents) were made at different locations on each of the samples with 9 μm spacing between each indentation. The average values were used as the E of the matrix for FEM calculations.

3. Computational techniques used

3.1. Scan-and-Solve meshfree method

To overcome difficulties in creating spatial meshes that can be used for stress analysis in porous materials, Scan-and-Solve approach is proposed [11,12], which is based on the Solution Structure Method [13–15]. The method makes it possible to construct solutions to the boundary value problems that satisfy all prescribed boundary conditions exactly. The main idea of the method is to represent the physical fields being modeled by powers of the functions that vanish on the geometric boundaries where the boundary conditions are prescribed [14]. In terms of stress analysis problems components of the displacement vector that satisfy kinematic boundary conditions can be written as follows [14]:

$$u_i = \omega_i \Phi_i + u_i^1, \quad i = x, y, z; \quad (1)$$

where ω_i are the functions that take on zero value on the boundaries which are fixed or on which known values of the displacement components u_i^1 are prescribed. The purpose of the functions Φ_i in the solution structure (1) is to provide the best approximation to the governing equation of the problem. Since in many practical situations Φ_i cannot be determined exactly, they are represented by a linear combinations of the basis functions:

$$\Phi_i = \sum_{j=1}^N C_j^i \chi_j \quad (2)$$

Representing the displacement components by the solution structure (1) allows to separate geometric information represented by zero sets of the functions ω_i and analytic information represented by functions Φ_i . As the result, the basis functions $\{\chi_j\}_{j=1}^N$ can be constructed over the spatial grids that do not necessarily conform to the shape of the geometric domain. This makes the Solution Structure Method essentially meshfree. Independence of the basis functions used to approximate the solution of the physical problem from the geometry for the computational domain

provides the Solution Structure Method with much higher level of flexibility in handling complex geometric domains in comparison with the traditional finite element methods. The solution structure (1) does not restrict the choice of the basis functions or the solution method used to determine numerical values of the degrees of freedom C_j^i .

Success and applicability of the Solution Structure Method to the real-world problems are determined to a large degree by the ability to construct smooth functions ω_i that vanish on the boundaries of an arbitrary complex geometric domain. In this paper we will use a Scan-and-Solve approach that provides capability to construct functions ω_i from acquired geometric models including images [11,12]. The construction process is illustrated in Fig. 1a–e. It starts with a 2D micrograph shown in Fig. 1a. In order to separate pores from the areas filled with the material, the image segmentation is performed. White color in the binary image in Fig. 1b corresponds to the areas filled with material while black color stands for the pores. Then a 2D Euclidean distance transform is performed over the binary image. It produces a piecewise constant distance field which can be visualized by a grayscale image where the intensity of the gray color defines the distance of each pixel from the nearest boundary pixel (Fig. 1c). In order to be used to construct displacements, the distance fields constructed using the distance transformation has to be smoothed out. This can be done by a number of ways. In this work, we constructed a smooth approximate distance field by applying a least square fit of B-splines to the gray color values in Fig. 1c. This results in a continuous smooth function ω (Fig. 1d) which mimics the behavior of the piecewise constant distance field in Fig. 1c. The zero set of ω , whose isolines are shown in Fig. 1d, approximates the boundary of the geometric domain. As it was illustrated in [16], the geometric accuracy provided by this approach is comparable with the physical size of a pixel in the micrograph. The described process constructs the approximate distance field ω for the whole boundary of the geometric domain. However, in practical situations we need to construct distance fields ω_i that correspond to the portions of the domain's boundary where the displacement values are prescribed. This can be achieved by using trimming operation [17] that combines the distance field for the whole boundary with distance-like functions for the boundaries of trimming volumes. The trimming volumes enclose the portions of the boundaries at which the displacement is known. Plot in Fig. 1e illustrates the result of the trimming operation. Blue¹ color in Fig. 1e corresponds to the boundaries where the displacement is specified. Functions u_i^1 (Fig. 1f) transfinately interpolate the prescribed values of the displacement [14]. Once ω_i and u_i^1 are constructed and the basis functions $\{\chi_j\}_{j=1}^N$ are chosen, a standard solution procedure can be applied [12,15].

3.2. Object oriented finite element method

Object oriented finite element technique (OOF) allows computation of the mechanical properties directly from the microstructure. It is becoming an increasingly popular tool for the computation of properties like thermal conductivity and elastic modulus of multi-phase materials with complex microstructures [18–21]. OOF can be implemented using the OOF2 software developed by Langer and co-workers at NIST [7,8]. It is based on the adaptive mesh technology which allows for generating finite element mesh conforming to the boundary of the phases in the microstructure. The different phases are selected based on their color or grayscale and different properties (electrical, thermal and mechan-

¹ For interpretation of color in Fig. 1, the reader is referred to the web version of this article.

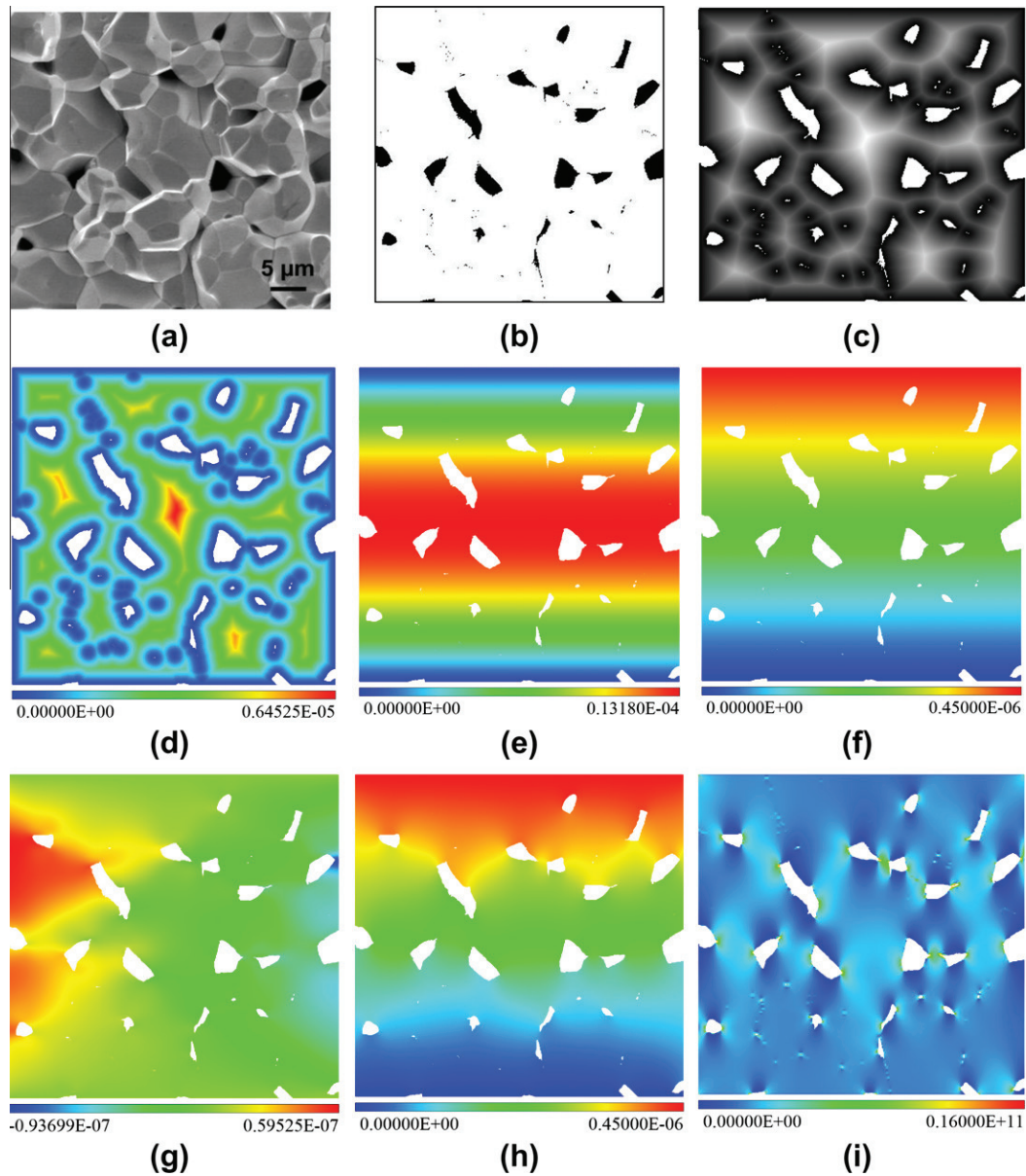


Fig. 1. Two-dimensional meshfree stress analysis from micrographs: (a) SEM micrograph of fracture surface of TaC-2200 sample. Image segmentation results in a binary image (b) where white color depicts material and black color corresponds to the pores. (c) Two-dimensional distance transformation results in an image, where intensity of the gray color depicts the distance to the nearest boundary pixel. (d) Least square fitting of B-splines to the gray values in (c) results in a smooth distance field. (e) Portions of the zero set of the distance field in (d) are used to specify boundary conditions for the analysis. Analysis results: (g, h) horizontal and vertical components of the displacement vector; (i) σ_y stress in porous ceramic material (shown on the scale from 0 to 16 GPa).

ical) can be assigned to each of these phases and the overall response of the microstructure to the boundary conditions can be obtained. Since the method is based on the actual microstructure, it takes into account the morphology of the phases and gives an accurate prediction of the overall properties. In the present study, the SEM images containing matrix and porosity regions (Figs. 1–3a) were converted into binary images (Fig. 1b) using Image J software. The binary images were then used in the OOF2 software and the mesh was created. The matrix was allotted properties obtained from nanoindentation and the porosities were allotted an elastic modulus of 10^{-8} GPa and a Poisson's ratio of 0.48. The value of Poisson's ratio for porosity was chosen assuming it to be very soft like elastomeric materials [22]. The stress distribution in the microstructure was then calculated for a boundary condition corresponding to a uniaxial tensile strain of 1%. The overall modulus

of the microstructure was calculated by dividing the integral stress at the boundary by the strain.

4. Results and discussion

Scan-and-Solve meshfree approach and object oriented finite element analysis methods were adopted to calculate stresses in TaC-2200 and TaC-BC-1850 microstructure for the same boundary conditions and then evaluate the overall elastic modulus. For both samples we have used two-dimensional plane stress formulation with the same loading conditions. The bottom boundary of the samples is fixed in both horizontal and vertical directions. On the upper boundary 1% strain in the vertical direction is applied.

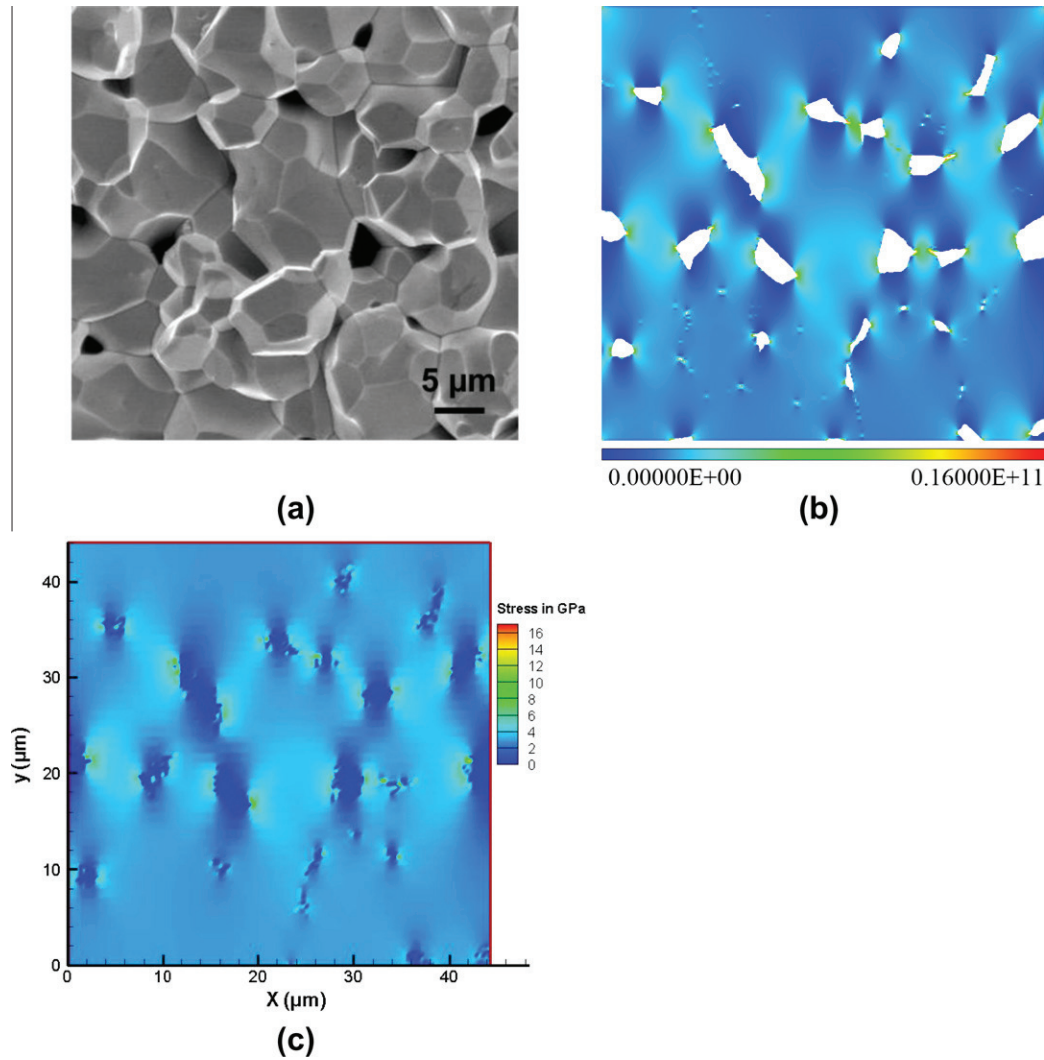


Fig. 2. (a) Micrograph of TaC-2200C sample. Distribution of the normal stress σ_y (shown on the scale from 0 to 16 GPa) obtained by (b) Scan-and-Solve meshfree method and (c) FEA implemented in OOF2 software.

Fig. 2 illustrates results of stress simulation in TaC-2200 sample. To perform the computations, we used the value of 283 GPa for the modulus of elasticity, which was obtained experimentally from the loading–unloading curve via nanoindentation. Poisson ratio was assigned the value of 0.24. Analysis of plots in Fig. 2b and c reveals that distribution of the normal stress σ_y obtained by the Scan-and-Solve meshfree method is very similar to the one obtained by the FEA implemented in OOF2 software. Since OOF2 software treats the pores as a separate material with a negligently low value of the modulus of elasticity, the normal stress σ_y in Fig. 2c is plotted over the whole computational domain including the voids where it vanishes. Scan-and-Solve meshfree method defines computational domain as a set of points where the signed distance field (Fig. 1d) is positive. To assemble the stiffness matrix and the load vector of the algebraic system, meshfree method employs geometrically adaptive numerical integration. In addition to the normal stress σ_y , porosity coefficient and effective modulus of elasticity have been computed by both methods. Porosity coefficient is a ratio of the volume occupied by the pores to the total volume of the sample. In the engineering practice it can be used to estimate the effective modulus of elasticity using the rule of mixture. Due to the random distributions of the pores, isotropic behavior of the homogenized material is assumed.

For the TaC-2200 sample, the porosity coefficient and the effective (homogenized) modulus of elasticity were calculated to be 6.2% and 224 GPa respectively by the Scan-and-Solve method. The corresponding values of the porosity coefficient and the effective modulus of elasticity determined by OOF2 software are 3% and 262 GPa respectively. The elastic modulus values are different due to the difference in the porosity coefficient. The lower elastic modulus value obtained by Scan-and-Solve method could be attributed to the higher measured porosity coefficient. It should be noted that overall computed elastic modulus is lower than those obtained experimentally via nanoindentation. This is due to the localized nature of indents which are made in the dense region and hence, do not account for the porosity. The rule of mixture estimates the values of the effective modulus of elasticity to be 265.45 GPa and 274.51 GPa for Scan-and-Solve and OOF2 methods respectively.

Results of stress simulations in TaC-BC-1850 sample are presented in Fig. 3. An experimental modulus value of 313 GPa was used as the input for both computational methods. As in the previous numerical experiment, both Scan-and-Solve meshfree method and FEA resulted in very similar distributions of the normal stress σ_y . The values of the porosity coefficient reported by the Scan-and-Solve and OOF2 methods are 3.7% and 4.2% respectively, and the

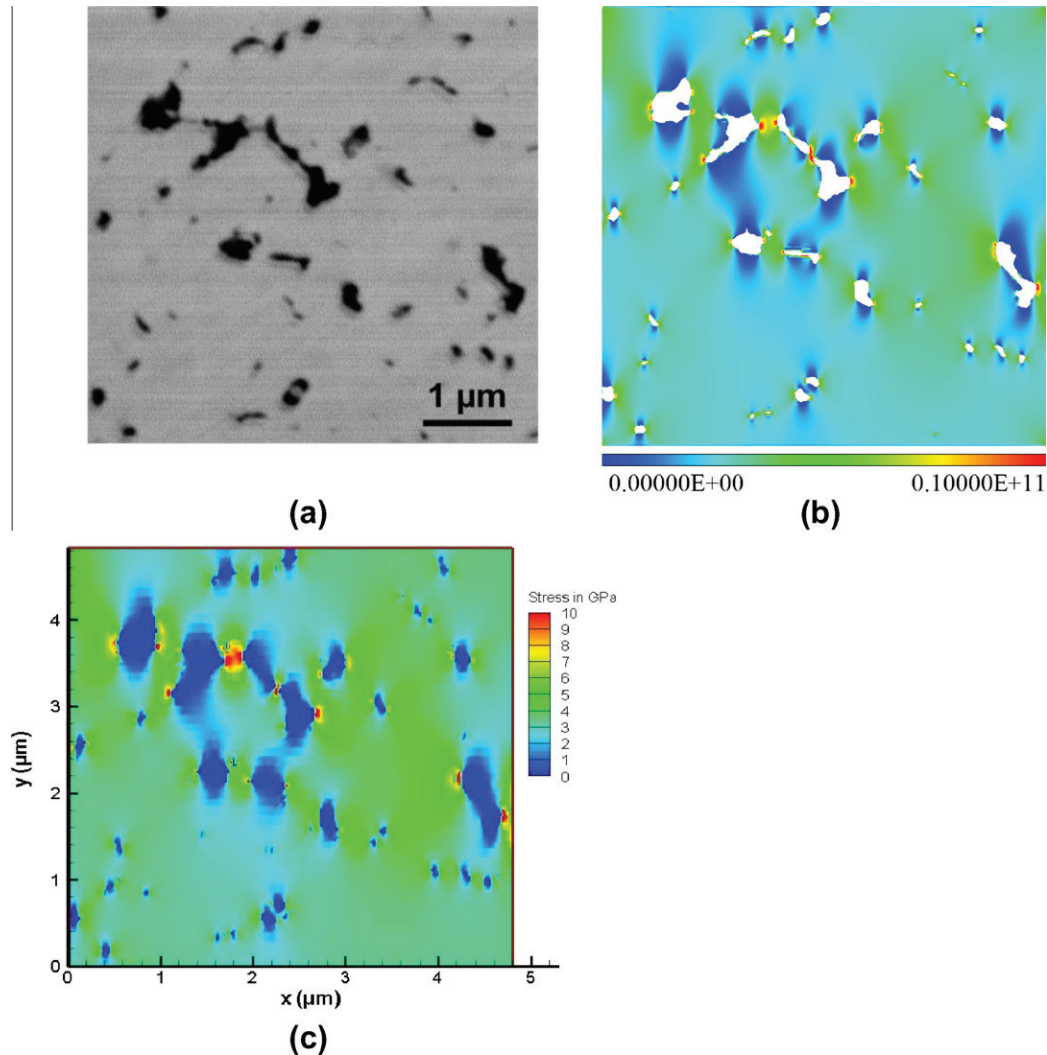


Fig. 3. (a) Micrograph of TaC-BC-1850 sample. Distribution of the normal stress σ_y (shown on the scale from 0 to 16 GPa) obtained by (b) Scan-and-Solve meshfree method and (c) FEA implemented in OOF2 software.

values of the effective modulus of elasticity are 266 GPa and 270 GPa. It is observed that since the porosity coefficient is similar as measured from both methods, the effective elastic modulus predicted is also quite similar. The rule of mixture estimates the values of the effective modulus of elasticity to be 301.42 GPa and 299.85 GPa for OOF2 and Scan-and-Solve methods respectively. The scale of the stress distribution as predicted by both these methods is also similar. This study proves that Scan-and-Solve method could be an effective and time-saving method for the prediction of overall properties from microstructure.

5. Conclusions

Meshfree Scan-and-Solve approach has a great potential to become a powerful computational tool for analyzing composite and porous materials *in situ*. The results on our preliminary numerical experiments and comparisons with traditional analysis techniques based on the finite element method demonstrate good agreement of the results obtained by both methods. However, the estimates of the effective modulus of elasticity given by the rule of mixture substantially differ from the obtained numerical results. The rule of mixture provides higher values of the effective modulus of elasticity. This difference can be explained by the fact that the rule

of mixture does not account for the physics of deformation, and therefore might not be reliable tool to determine the mechanical properties of the homogenized materials. The presented meshfree method possesses good numerical properties. In particular, it guarantees exact treatment of all prescribed boundary conditions at every point on the geometric boundary. The big advantage of the presented Scan-and-Solve meshfree method over traditional mesh-based analysis methods is complete automated solution procedure which can be extended into 3D space. The method can perform analysis from 2D segmented micrographs as well as from segmented 3D Computed Tomography (CT) scans. Extension of the numerical computations into 3D will eliminate the errors introduced by 2D analysis. In the reality, pores have complex three-dimensional shape that cannot be captured from a 2D SEM micrograph (such as show in Fig. 1a). In this case two-dimensional numerical analysis assumes that the shape of pores does not change in the third dimension.

Acknowledgments

A.A. acknowledges the financial support from the Air Force Office of Scientific Research (FA9550-09-1-0297). This research was also supported in part by the National Science Foundation

Grant CMMI-0900219 (IT). Authors also thank Dr. Steve Langer at NIST for his assistance with the installation of the OOF software.

References

- [1] F. Cernuschi, S. Ahmaniemi, P. Vuoristo, T. Mantyla, J. Eur. Ceram. Soc. 24 (2004) 2657–2667.
- [2] A. Bjorneklett, L. Haukeland, J. Wigren, H. Kristiansen, J. Mater. Sci. 29 (1994) 4043–4050.
- [3] G. Ondracek, B. Schulz, J. Nucl. Mater. 46 (1973) 253–258.
- [4] R. Landauer, J. Appl. Phys. 23 (1952) 779–784.
- [5] C.-W. Nan, G. Liu, Y. Lin, M. Li, Appl. Phys. Lett. 85 (2004) 3549–3551.
- [6] S.R. Bakshi, R.R. Patel, A. Agarwal, Comput. Mater. Sci. 50 (2010) 419–428.
- [7] A.C.E. Reid, S.A. Langer, R.C. Lua, V.R. Coffman, S.-I. Haan, R.E. Garcia, Comput. Mater. Sci. 43 (2008) 989–999.
- [8] A.C.E. Reid, R.C. Lua, R.E. Garcia, V.R. Coffman, S.A. Langer, Int. J. Mater. Prod. Technol. 35 (2009) 361–373.
- [9] S. Li, W.K. Liu, Appl. Mech. Rev. 55 (2002) 1–34.
- [10] S.R. Bakshi, V. Musaramthota, D. Lahiri, V. Singh, S. Seal, A. Agarwal, Mater. Sci. Eng. A, doi:10.1016/j.msea.2010.10.009.
- [11] M. Freytag, V. Shapiro, I. Tsukanov, Comput. Aided Des. 38 (2006) 87–100.
- [12] M. Freytag, V. Shapiro, I. Tsukanov, Scan and solve: acquiring the physics of artifacts, in: Proceedings on 2007 ASME International Design Engineering Technology Conference 2007, Las Vegas, NV, USA.
- [13] V.L. Rvachev, T.I. Sheiko, V. Shapiro, I. Tsukanov, Comput. Mech. 25 (2000) 305–316.
- [14] V.L. Rvachev, T.I. Sheiko, V. Shapiro, I. Tsukanov, Comput. Aided Geom. Des. 18 (2001) 195–220.
- [15] I. Tsukanov, V. Shapiro, Adv. Comput. Math. 23 (2005) 95–124.
- [16] M. Freytag, V. Shapiro, I. Tsukanov, Differentiable Distance Fields from Scanned Data, SAL Technical Report 2007. <<http://sal-cnc.me.wisc.edu>>.
- [17] V. Shapiro, I. Tsukanov, Implicit functions with guaranteed differential properties, in: Proceedings of the Fifth ACM Symposium on Solid Modeling and Applications, June 1999, Ann Arbor, MI, pp. 258–269.
- [18] Y. Dong, D. Bhattacharyya, P.J. Hunter, Comput. Sci. Technol. 68 (2008) 2864–2875.
- [19] A. Goel, K.K. Chawla, U.K. Vaidya, N. Chawla, M. Koopman, Mater. Sci. Technol. 24 (2008) 864–869.
- [20] A.D. Jadhav, N.P. Padture, E.H. Jordan, M. Gell, P. Miranzo, E.R. Fuller Jr., Acta Mater. 54 (2006) 3343–3349.
- [21] Z. Wang, A. Kulkarni, S. Deshpande, T. Nakamura, H. Herman, Acta Mater. 51 (2003) 5319–5334.
- [22] J.-H. Yu, D.A. Dillard, D.R. Lefebvre, Int. J. Solids Struct. 38 (2001) 6839–6849.